



Absorbing aerosols over Asia: A Geophysical Fluid Dynamics Laboratory general circulation model sensitivity study of model response to aerosol optical depth and aerosol absorption

C. A. Randles^{1,2} and V. Ramaswamy^{1,3}

Received 17 March 2008; revised 9 June 2008; accepted 1 August 2008; published 5 November 2008.

[1] Forcing by absorbing atmospheric black carbon (BC) tends to heat the atmosphere, cool the surface, and reduce the surface latent and sensible heat fluxes. BC aerosol can have a large impact on regional climates and the hydrologic cycle. However, significant uncertainties remain concerning the increases in (1) the total amount of all aerosol species and (2) the amount of aerosol absorption that may have occurred over the 1950–1990 period. Focusing on south and east Asia, the sensitivity of a general circulation model's climate response (with prescribed sea surface temperatures and aerosol distributions) to such changes is investigated by considering a range of both aerosol absorption and aerosol extinction optical depth increases. We include direct and semidirect aerosol effects only. Precipitation changes are less sensitive to changes in aerosol absorption optical depth at lower aerosol loadings. At higher-extinction optical depths, low-level convergence and increases in vertical velocity overcome the stabilizing effects of absorbing aerosols and enhance the monsoonal circulation and precipitation in northwestern India. In contrast, the presence of increases in only scattering aerosols weakens the monsoonal circulation and inhibits precipitation here. Cloud amount changes can enhance or counteract surface solar flux reduction depending on the aerosol loading and absorption, with the changes also influencing the surface temperature and the surface energy balance. The results have implications for aerosol reduction strategies in the future that seek to mitigate air pollution concerns. At higher optical depths, if absorbing aerosol is present, reduction of scattering aerosol alone has a reduced effect on precipitation changes, implying that reductions in BC aerosols should be undertaken at the same time as reductions in sulfate aerosols.

Citation: Randles, C. A., and V. Ramaswamy (2008), Absorbing aerosols over Asia: A Geophysical Fluid Dynamics Laboratory general circulation model sensitivity study of model response to aerosol optical depth and aerosol absorption, *J. Geophys. Res.*, *113*, D21203, doi:10.1029/2008JD010140.

1. Introduction

[2] Since pre-industrial times, increasing concentrations of tropospheric greenhouse gases (GHGs) such as carbon dioxide (CO₂) and methane (CH₄) have perturbed the radiative balance of the Earth-atmosphere system by trapping outgoing infrared radiation, causing the climate to warm. Concurrently, increases in atmospheric aerosols, which directly affect climate through the absorption and scattering of incoming solar radiation and indirectly affect climate through microphysical interactions with clouds, have also contributed to a perturbation of the radiative balance of the Earth-

atmosphere system [Solomon *et al.*, 2007]. Nonabsorbing aerosol species such as sulfate (SO₄) and organic carbon (OC) primarily scatter sunlight and reduce the amount of solar radiation reaching the surface, contributing to surface cooling [Ramanathan *et al.*, 2001a]. Black carbon (BC) aerosol, which is produced from the incomplete combustion of biomass and fossil fuels, however, both scatters and absorbs incoming solar radiation. As a result, BC contributes to a reduction of solar flux at the surface while simultaneously heating the atmosphere [Ramaswamy *et al.*, 2001]. Recent studies have begun to recognize BC as an important contributor to global climate change [e.g., Hansen and Nazarenko, 2004; Chung and Seinfeld, 2005] and to regional climate change [e.g., Ramanathan *et al.*, 2001b; Chung *et al.*, 2002; Menon *et al.*, 2002; Lau and Kim, 2006]. Because BC aerosol alters the partitioning of energy between the surface and the atmosphere, it can act to stabilize the atmosphere and modulate the hydrologic cycle [Ramanathan *et al.*, 2005]. BC aerosol may also reduce cloud cover as it absorbs solar radiation and heats the atmosphere, the so-called semidirect effect [Hansen *et al.*, 1997]. The semidirect effect amplifies

¹Atmospheric and Oceanic Sciences Program, Princeton University, Princeton, New Jersey, USA.

²Now at NASA Goddard Space Flight Center, Greenbelt, Maryland, USA.

³Geophysical Fluid Dynamics Laboratory, NOAA, Princeton, New Jersey, USA.

the warming associated with absorbing BC aerosols by reducing low-level clouds, which would otherwise contribute to atmospheric scattering and surface cooling [Johnson *et al.*, 2004].

[3] Over the past half century, there have been dramatic increases in anthropogenic aerosols in the Asian region. Accompanying the increase in scattering anthropogenic aerosols (e.g., sulfates), large industrial emissions and the widespread use of low-efficiency domestic burning have made south and east Asia some of the largest producers of carbonaceous aerosols (absorbing BC and mostly scattering OC) [Wu *et al.*, 2004; Zhao *et al.*, 2006a]. Recent equilibrium model studies using prescribed sea surface temperatures (SSTs) indicate that absorbing BC aerosol loading may contribute to regional precipitation changes in India and China. For example, using model aerosol properties based on observations, Chung *et al.* [2002] and Menon *et al.* [2002] have shown that atmospheric absorption associated with increases in absorbing aerosols may have increased average precipitation over India and China. Similarly, Lau *et al.* [2006] show that increases in absorbing aerosols over northern India and the Tibetan Plateau, a region of high surface albedo, lead to anomalous heating. This heating accentuates the elevated heat source of the Plateau and acts as an “Elevated Heat Pump” (EHP). The EHP enhances the meridional temperature gradient, and contributes to an enhanced Indian monsoon with increased rainfall over India during the late spring and early summer. However, when SSTs are allowed to respond to aerosol surface forcing (such as in a coupled ocean-atmosphere model), the impact of aerosols on the monsoon may be different. Ramanathan *et al.* [2005] and Chung and Ramanathan [2006] conclude that reductions in surface solar radiation from increased absorbing and scattering aerosols suppress the GHG warming of SSTs more in the northern Indian Ocean than in the southern Indian Ocean. This weakening of the SST gradients since the 1950s has led to a deceleration of the summer monsoon circulation, decreases in evaporation, and increases in atmospheric stability that have reduced rainfall over India during the summer. Owing to the thermal capacity of the ocean, however, this effect on the north-south SST gradient lags the peak in aerosol surface solar flux reduction in the spring (premonsoon period), and the monsoon does not weaken until the summertime [Ramanathan and Carmichael, 2008].

[4] The aforementioned studies reveal that there remain ambiguities regarding the relative climatic influence of absorbing and scattering aerosol components in the Asian region. The impact of aerosols on the monsoon likely depends on a balance between aerosol “EHP” effects (i.e., enhanced monsoon associated with increased atmospheric shortwave heating from absorbing aerosols) and the SST gradient effects (i.e., decelerated monsoon associated with decreased surface flux from both scattering and absorbing aerosols). Understanding this balance is difficult, in part, owing to a lack of knowledge about the spatial and temporal evolution of aerosol extinction and absorption optical depths. There is a paucity of observations of aerosol properties spanning the last half century in this region. There is also a lack of model-based quantification of aerosol properties in the Asian region, and there is a poor understanding of the sensitivity of the models’ response to changes in aerosol

parameters. This motivates the experimental strategy for this study.

[5] Using the Geophysical Fluid Dynamics Laboratory (GFDL) general circulation model (GCM), we explore the sensitivities of the Asian regional climate response to changes in aerosol radiative forcing over India and China associated with increases in both absorbing and scattering anthropogenic aerosols (BC, SO₄, and OC), as are likely to have occurred over the second half of the 20th century [Ramaswamy *et al.*, 2001; Menon *et al.*, 2002]. In particular, this study is concerned with the sensitivity of the climate response to changes in anthropogenic aerosol extinction optical depth (τ_e ; the sum of the absorption optical depth (τ_a) and scattering optical depth (τ_s)) and to changes in the aerosol absorption optical depth (τ_a), and thus to changes in the ratio of scattering-to-extinction optical depths, namely, the single scattering albedo ω_0 . The extinction optical depth and single scattering albedo are two of the most important optical parameters governing aerosol climate forcing [Ramaswamy *et al.*, 2001].

[6] In these sensitivity experiments, only the direct and semidirect effects of tropospheric aerosols are explicitly accounted for; other effects, such as the first and second indirect aerosol effects pertaining to the interaction of aerosols with cloud albedo and cloud lifetime, are not considered. Because SSTs are prescribed in our experiments, we can only in essence examine the sensitivity of the Asian climate to changes in aerosol heating (e.g., “EHP” effects) associated with changes in τ_e and τ_a . This study is thus an essential and systematic first step at understanding the range in model sensitivity to changes in aerosol optical parameters before progressing to more complicated solutions (e.g., mixed-layer ocean or fully coupled ocean). We test the model’s response to variations in aerosol absorption by considering different assumptions of “1990” τ_e and τ_a compared to a “1950” control experiment. In section 2 we describe the model, the experimental design, and the aerosol optical properties for each perturbation experiment. In section 3 we compare aerosol direct radiative forcing and direct radiative efficiency over India and China to observations. In section 4.1 and 4.2, we discuss the air temperature, hydrologic cycle, and surface energy balance response of the model to the perturbation experiments over India and China, respectively. A summary and discussion are given in section 5, and the final conclusions are given in section 6.

2. Methodology

2.1. Climate Model: GFDL AM2-LM2 GCM

[7] The GFDL atmospheric-land GCM AM2-LM2 has a hydrostatic, finite-difference dynamical core [Lin, 2004] with a horizontal grid set to N45 resolution (2.5° longitude \times 2.0° latitude) and 24 vertical levels (9 in the lowest 1.5 km, 2-km resolution in the upper troposphere, and 5 levels in the stratosphere) on a hybrid coordinate grid (sigma surfaces near the ground continuously transform to pressure surfaces above 250 hPa). Prognostic variables include zonal and meridional wind components, surface pressure, temperature, and tracers (e.g., specific humidity of water vapor and the prognostic cloud variables of cloud liquid, cloud ice, and cloud fraction). The land model LM2 includes soil sensible

and latent heat storage, groundwater storage, and stomatal resistance. *Anderson et al.* [2004] give a complete overview of the AM2-LM2 GCM physical parameterizations, including the treatment of scattering and absorption of radiation by aerosols, and model evaluation for a series of prescribed SST simulations. Here we only describe those aspects of the AM2-LM2 GCM that are relevant to aerosols.

[8] Off-line three-dimensional monthly mean mass profiles of five aerosol species (SO_4 , BC, OC, dust, and sea salt) are prescribed and linearly interpolated between months. Optical properties for each species (specific extinction coefficient α_e , single scattering albedo ω_o , and asymmetry parameter g) are determined off-line for 40 wavelengths using Mie theory and assumed aerosol size distributions, refractive indices, particle density, and hygroscopic properties [*Haywood and Ramaswamy*, 1998; *Haywood et al.*, 1999]. The effects of hygroscopic growth with increasing RH on optical properties are considered for sea salt and sulfate aerosol. For sea salt, the aerosol is assumed to be in an environment of constant 80% relative humidity, while sulfate optical properties vary with the calculated relative humidity from AM2-LM2 (up to 100% RH). Between 30% and 80% RH, the hygroscopic growth of SO_4 follows the method of *Haywood and Ramaswamy* [1998] and between 80% and 100% RH it follows the approximation of *Fitzgerald* [1975]. The total aerosol extinction optical depth τ_e is calculated by assuming an external mixture and summing the contribution of each aerosol species i to the optical depth, which is given by the product of the aerosol column mass burden M and the specific extinction coefficient ($\tau_e = \sum_i \tau_{e,i} = \sum_i M_i \alpha_{e,i}$ where i represents SO_4 , BC, OC, dust, and sea salt). Note that, other than changes in relative humidity, changes in model dynamics (e.g., precipitation) do not feed back onto aerosol optical properties because aerosol mass distributions are prescribed.

2.2. Experimental Design

[9] We design a set of numerical experiments for the GFDL AM2-LM2 GCM to investigate the climate response to increased anthropogenic aerosol extinction and to changes in the proportion of aerosol absorption over roughly the last 50 years. We use available present-day observations of aerosol optical properties to constrain the range of the parameters τ_e and ω_o , and we difference results of each experiment relative to a 1950 control (BASE) case. Each of the simulations and the BASE case differ from one another *only* in their anthropogenic (i.e., BC, OC, and SO_4) aerosol distributions. SSTs, sea-ice, long-lived GHGs, ozone, and land-surface properties are identical for all simulations. SSTs and sea ice are prescribed as climatological monthly means corresponding to the average over the period 1981 to 1999 [*Reynolds et al.*, 2002]. Long-lived GHGs and ozone are fixed at their 1950 concentrations. The mass distributions of the natural aerosol species (i.e., dust and sea salt) are the same for all simulations. SSTs, sea ice, and natural aerosols, while fixed from year to year in a given simulation, vary seasonally. The OC in this version of the GFDL GCM is scattering and nonhygroscopic, while SO_4 is scattering and nominally treated as hygroscopic between 30% and 100% RH (unless noted otherwise). BC is the only absorbing component of the anthropogenic aerosol. All equilibrium simulations were run for 35 years and results averaged over the last 30 years. We assess the significance

of modeled climate response using the student's t-test. For the purpose of the t-test, the degree of freedom was prescribed as $178 (3 \text{ months} \times 30 \text{ years of experiment} + 3 \text{ months} \times 30 \text{ years of BASE} - 2)$ following *Erlick et al.* [2006]. Note that the significance level computed with the t-test indicates the significance of the experiment's response with respect to the internal variability of the model; it is not a measure of the accuracy of the model.

[10] We design a series of six sensitivity experiments that are divided into two regimes on the basis of their relative increases in anthropogenic extinction optical depth compared to the BASE case: the low optical depth regime (LOD) and the high optical depth regime (HOD). For the BASE case, with the exception of sea salt, whose profile is prescribed following *Haywood et al.* [1999], aerosol monthly mean mass profiles are prescribed from off-line simulations of the Model of OZone And Related chemical Tracers version 2 (MOZART-2) chemical transport model (CTM) for the year 1950 [*Horowitz*, 2006]. Note that in the naming convention for the perturbation experiments (denoted by "X"), a lowercase "a" stands for ambient (i.e., SO_4 is not hygroscopic and optical properties of SO_4 are fixed at 30% RH), a lowercase "h" indicates that SO_4 is hygroscopic (optical properties of SO_4 are a function of model RH between 30% and 100% RH), and an uppercase "W" indicates that the anthropogenic aerosol is "white" or purely scattering. For the remainder of this study, Δ will refer to the change in a given parameter between experiment X and the BASE case (i.e., X - BASE). Because the natural aerosol optical depth does not vary between the experiments and the BASE case, $\Delta\tau_e$ represents the increase in anthropogenic aerosol extinction optical depth between 1950 and the different assumptions for 1990 aerosols, and $\Delta\tau_a$ is the increase (or decrease) in anthropogenic aerosol absorption optical depth.

[11] Table 1 lists the simulated summertime (JJA) column-integrated, area-weighted average total aerosol (natural plus anthropogenic) visible ω_o , τ_e , and τ_a over India ($4^\circ\text{S} - 32^\circ\text{N}$, $65^\circ\text{E} - 90^\circ\text{E}$) and China ($20^\circ\text{N} - 54^\circ\text{N}$, $90^\circ\text{E} - 130^\circ\text{E}$) for the BASE case and the six experiments. Table 1 also lists present-day available observations of ω_o and τ_e from various field campaigns and remote sensing platforms. Within each regime, ω_o varies between a low of 0.85 (highly absorbing) and a high approaching 1 (highly scattering). We note that a ω_o of 0.85 is representative of the most absorbing observations found in this region [*Ramanathan et al.*, 2001b; *Clarke et al.*, 2004], though even higher absorption has been observed in industrialized urban areas [e.g., *Babu et al.*, 2002; *Tripathi et al.*, 2005]. The measurements of ω_o presented in Table 1 typically represent ambient aerosols irrespective of the method by which the observations were made (i.e., measurements made at reduced RH were typically adjusted using models to match ambient RH conditions or the measurements in Table 1 represent a field campaign average from several different experimental techniques).

[12] In the LOD regime (XA, XBa, and XBh), the aerosol anthropogenic mass increases between 1950 and 1990 are consistent with simulations from MOZART-2 [*Horowitz*, 2006]. For the present-day period, the MOZART-2 aerosol mass distributions combined with the AM2-LM2 aerosol optical properties result in an

Table 1. June/July/August Column-Integrated Aerosol Optical Properties^a

| | Single Scattering Albedo (ω_o) | Extinction Optical Depth (τ_e) | Absorption Optical Depth (τ_a) ($\times 10^{-2}$) |
|--------------|--|--|--|
| <i>India</i> | | | |
| BASE | 0.89 (0.85) | 0.15 (0.18) | 1.90 (2.69) |
| LOD | | | |
| XA | 0.91 (0.89) | 0.25 (0.34) | 2.45 (3.79) |
| XBa | 0.85 (0.83) | 0.17 (0.22) | 2.52 (3.81) |
| XBh | 0.90 (0.88) | 0.24 (0.34) | 2.52 (3.81) |
| HOD | | | |
| XCa | 0.85 (0.83) | 0.56 (0.59) | 8.71 (9.87) |
| XCh | 0.93 (0.91) | 1.27 (1.17) | 8.71 (9.87) |
| XChW | 0.99 (0.98) | 1.15 (1.04) | 1.46 (1.81) |
| Observations | 0.85–0.9 ^b | 0.17–1.28 ^c | — |
| | 0.87–0.94 ^d | 0.12–0.24 ^e | — |
| | 0.7–0.9 ^f | 0.42 (0.62) ^g | — |
| <i>China</i> | | | |
| BASE | 0.90 (0.89) | 0.15 (0.15) | 1.50 (1.65) |
| LOD | | | |
| XA | 0.94 (0.93) | 0.44 (0.45) | 2.70 (2.84) |
| XBa | 0.85 (0.84) | 0.22 (0.22) | 3.41 (3.54) |
| XBh | 0.92 (0.92) | 0.43 (0.44) | 3.41 (3.54) |
| HOD | | | |
| XCa | 0.85 (0.84) | 0.54 (0.59) | 8.32 (9.28) |
| XCh | 0.93 (0.93) | 1.16 (1.31) | 8.32 (9.28) |
| XChW | 0.99 (0.99) | 1.09 (1.23) | 0.83 (0.93) |
| Observations | 0.84–0.96 ^h | 0.48–1.37 ⁱ | — |
| | 0.83–0.99 ^j | 0.41 (0.42) ^g | — |

^aLand and ocean average with land-only average in parentheses.

^bINDOEX field campaign (January–March 1999) [Ramanathan *et al.*, 2001a].

^cKanpur, India AERONET station (2001–2007, JJA range).

^dManora Peak in the central Himalayas (December 2004) [Pant *et al.*, 2006].

^eNorthern Indian Ocean (Kaashidhoo) AERONET station (1998–2000, JJA range).

^fNepal (December–February 2003) [Ramana *et al.*, 2004].

^gMODIS (2002–2004) JJA average (standard deviation).

^hACE Asia field campaign (March–May 2001) [Huebert *et al.*, 2003].

ⁱMainland China (Beijing) AERONET station (2002–2007, JJA range).

^jEAST-AIRE field campaign (June–August 2005) [Lee *et al.*, 2007].

underestimate in modeled τ_e over India and China between ~25 and 100% in the annual mean [Ginoux *et al.*, 2006] relative to observations from the ground-based Aerosol Robotic Network (AERONET) of sun photometers [Holben *et al.*, 2001]. In the LOD experiments, τ_e increases relative to the BASE case by roughly a factor of 2 over land in India and by roughly a factor of 3 over land in China (Table 1). Our results indicate that the changes in the model's hydrologic cycle and surface air temperature response are generally not significant above the 90% confidence level for the LOD changes in τ_e and ω_o considered. We therefore focus the remainder of this study on results from the HOD experiments and reserve discussion of the LOD experiments for the auxiliary material.¹ However, we retain XA to serve as a basic contrast between the general aspects of the LOD experiments and the HOD experiments. XA uses the MOZART-2 BC, OC, and SO₄ aerosol mass distributions for the year 1990 [Horowitz, 2006], and the same sea

salt and dust mass distributions as the BASE case as described previously. Sulfate aerosols are treated as hygroscopic in XA.

[13] To construct HOD experiment XCa, the total anthropogenic aerosol mass distributions from MOZART-2 for the year 1990 (XA) were scaled up over India and China to obtain an aerosol extinction optical depth increase similar to Figure 1 of Menon *et al.* [2002]. At the same time, the mass of BC was increased relative to the mass of SO₄ + OC to maintain $\omega_o \leq 0.85$ at 550 nm over both India and China. Because XCa was designed by adjusting the dry aerosol masses, in order to maintain the τ_e from Menon *et al.* [2002] and to maintain $\omega_o \leq 0.85$, it was necessary to keep SO₄ optical properties fixed at 30% RH in the model runs. Fixing SO₄ optical properties at 30% RH also was done to enable an appropriate comparison with the Menon *et al.* [2002] study. For XCh, the same aerosol mass distributions used in XCa are employed, but SO₄ is hygroscopic between 30% and 100% RH. XCa and XCh share the same τ_a since their BC mass distributions are the same. However, τ_s (and thus τ_e and ω_o) differs between these two experiments owing to the treatment of sulfate hygroscopicity. XCh was designed to explore the effects of maintaining τ_a from XCa while increasing τ_s . Finally, for XChW, the same aerosol mass distributions from XCa are used, SO₄ is hygroscopic (30–100% RH), and the optical properties of BC are artificially set to the optical properties of SO₄ at 30% RH (essentially treating the BC mass as dry SO₄ and thus making the anthropogenic aerosol “white” or purely scattering and $\Delta\tau_a < 0$). The resulting τ_e for XChW is comparable to that of XCh because the extinction optical depth is dominated by (hygroscopic) sulfate extinction, which is roughly the same for both of these experiments (slight variations may exist owing to variations in model RH).

[14] With the exception of the hypothetical simulation XChW, ω_o for the six experiments clearly falls within the present-day observed range of ω_o (Table 1) over both India and China. The extinction optical depth for each sensitivity simulation also falls within the range of τ_e from the observations, though XCh and XChW overestimate considerably the area-mean observed τ_e . We also note that the all-sky (cloudy) top of the atmosphere (TOA) anthropogenic direct radiative forcings (DRF) for XCh and XChW are almost equal in magnitude but opposite in sign over both

Table 2. June/July/August All-Sky (Clear-Sky) Direct Radiative Forcings^a

| Experiment | TOA | ATM | SFC | SFC/TOA |
|---------------------------|---------------|---------------|---------------|--------------|
| <i>India</i> ^b | | | | |
| BASE | +1.9 (−0.4) | +4.2 (+3.8) | −2.3 (−4.2) | −1.2 (+10.5) |
| XA | +3.2 (−3.9) | +10.1 (+9.1) | −6.9 (−13.0) | −2.2 (+3.3) |
| XCa | +16.8 (−2.0) | +38.5 (+34.3) | −21.7 (−36.3) | −1.3 (+18.2) |
| XCh | +14.4 (−12.0) | +38.5 (+34.2) | −24.1 (−46.2) | −1.7 (+3.9) |
| XChW | −11.3 (−24.6) | ≈0 (≈0) | −11.3 (−24.7) | ≈1 (≈1) |
| <i>China</i> ^b | | | | |
| BASE | +0.5 (−1.5) | +2.9 (+2.7) | −2.4 (−4.2) | −4.8 (+2.8) |
| XA | +1.0 (−10.8) | +9.1 (+8.3) | −8.1 (−19.1) | −8.1 (+1.8) |
| XCa | +13.6 (−4.8) | +37.7 (+36.5) | −24.1 (−41.3) | −1.8 (+8.6) |
| XCh | +10.4 (−19.4) | +37.5 (+35.7) | −27.1 (−55.1) | −2.6 (+2.8) |
| XChW | −13.6 (−34.4) | ≈0 (≈0) | −13.6 (−34.4) | ≈1 (≈1) |

^aUnit is W m^{−2}. All-sky anthropogenic (OC + BC + SO₄) direct radiative forcings (DRF) with clear-sky DRF in parentheses.

^bLand-area average only.

¹Auxiliary materials are available in the HTML. doi:10.1029/2008JD010140.

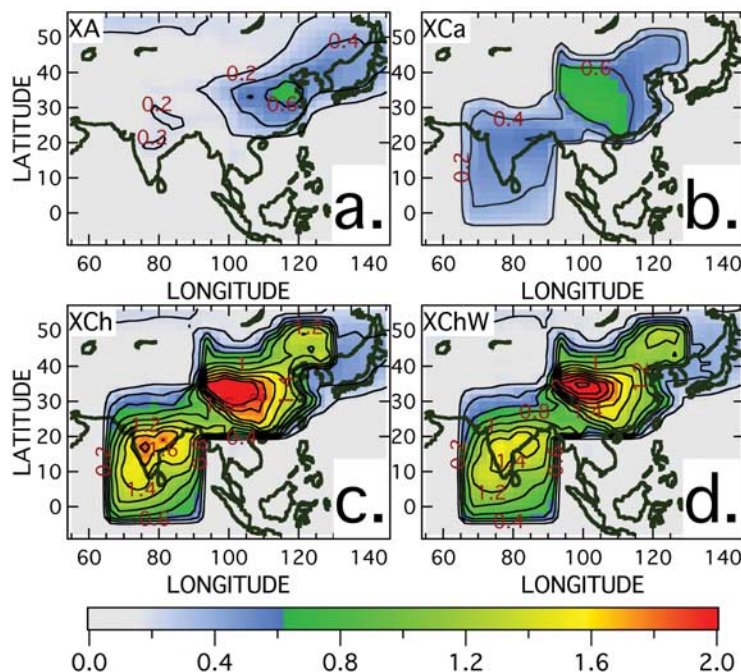


Figure 1. Column-integrated aerosol optical depth for each experiment differenced with respect to the BASE case ($\Delta\tau_e$): (a) XA, (b) XCa, (c) XCh, and (d) XChW. Note that this optical depth represents only the anthropogenic (BC, OC, and SO_4) aerosol component (increase between 1950 and 1990) since the natural (dust and sea salt) component is shared with the BASE case. The contour interval is 0.2.

India and China (see Table 2), making these experiments ideal candidates with which to contrast the impacts of increased absorbing and scattering aerosols, respectively.

[15] Figure 1 shows the difference in column-integrated visible extinction optical depth between the experiments and BASE ($\Delta\tau_e$) in summer (JJA). $\Delta\tau_e$ for XA (Figure 1a) is significantly less than the increase in aerosol extinction in the HOD experiments. The $\Delta\tau_e$ for XCa (Figure 1b) is similar to Figure 1 of Menon *et al.* [2002] and represents measured extinction optical depths over China (surface solar radiation observations during the 1990s [Luo *et al.*, 2001]) and chemical transport model assimilation of satellite retrievals of τ_e during INDOEX over India (1999 [Collins *et al.*, 2001]). XCh (Figure 1c) has a higher $\Delta\tau_e$ than XCa owing to SO_4 humidification (but $\Delta\tau_a$ is the same for these two experiments). The purpose behind introducing XChW (Figure 1d) is to strike a deliberate contrast with the more absorbing experiments XCa and XCh while maintaining a $\Delta\tau_e$ comparable to XCh. XChW can be considered to be a circumstance in which only the scattering aerosol component (e.g., sulfate) is present, and this experiment represents a hypothetical case, at least in the context of the contemporary atmosphere. The main aim for this experiment is to flush out the contrasts with the absorbing aerosol simulations.

[16] The experimental design adopted here is similar to that of Menon *et al.* [2002], particularly for XCa which uses the same τ_e and ω_o as Menon *et al.* [2002]. However, this study considers the sensitivity of radiative forcing and model response to changes in τ_a (and thus ω_o) at both lower and higher-extinction optical depths, encompassing the range in observations of these parameters, thus extending the scope compared to the earlier study. This design offers the opportunity to study the sensitivity of an entirely

different GCM to increased absorption and extinction optical depths, variables that are considerably uncertain and poorly quantified, over south and east Asia. Differencing the experimental results with respect to the BASE case captures the forcing due solely to the anthropogenic aerosol and allows us to examine the model response associated with a change from 1950 to different assumptions of 1990 anthropogenic aerosols.

3. Aerosol Direct Radiative Forcing and Direct Radiative Efficiency

[17] Climate response can be conceptualized as a two-stage process consisting of (1) the initial or direct radiative forcing (DRF) by a perturbing agent and (2) the climate response to that forcing, which includes climate feedback processes [Cess, 1985]. Here we define the direct radiative forcing (DRF) as the *instantaneous* change (down minus up) in radiative flux caused by the addition of a perturbing agent, which in this case is anthropogenic aerosol (i.e., the instantaneous flux change with anthropogenic aerosols minus without aerosols averaged over the diurnal cycle). Note that for tropospheric aerosols which interact primarily with shortwave radiation, such as BC, OC, and SO_4 , instantaneous forcing at the top of the atmosphere (TOA) and adjusted forcing as defined by the Intergovernmental Panel on Climate Change (IPCC) [Ramaswamy *et al.*, 2001] are approximately equal [Hansen *et al.*, 1997]. Here we examine the TOA, surface (SFC), and atmospheric (ATM) instantaneous anthropogenic direct radiative forcing over India and China, where the TOA forcing is the sum of the ATM and SFC forcings. SFC radiative forcing is a useful measure of climate response for absorbing aerosols and the

hydrologic cycle [e.g., Menon *et al.*, 2002], and the vertical structure of forcing (ATM) is useful for evaluating temperature change in the atmosphere.

[18] For XA and XCh, the clear-sky anthropogenic aerosol TOA DRFs over India given in Table 2 are a factor of 3 to 4 lower than the surface forcing, in agreement with findings from the INDOEX field campaign [Chung *et al.*, 2002]. For XCa, however, the clear-sky SFC forcing is ~ 18 times TOA clear-sky forcing over India and ~ 9 times TOA clear-sky forcing over China. This is because the high absorption throughout the atmosphere greatly decreases the upward flux at the TOA and the downward flux at the SFC, producing a weak forcing at the TOA relative to a strong negative forcing at the surface [Erlick *et al.*, 2006]. Also, for INDOEX, the absorbing aerosol layer was located within the lowest 3 km of the atmosphere, while in XCa absorbing aerosol extends throughout the troposphere owing to the preservation of the vertical profile of 1990 MOZART-2 anthropogenic aerosols in all the experiments (and the subsequent scaling of aerosol mass to obtain τ_e from Menon *et al.* [2002]). XChW has a ratio of clear-sky SFC to TOA anthropogenic forcing close to one because the ATM forcing is negligible, whereas ATM forcing is positive for the other simulations.

[19] Table 2 also presents the area-averaged all-sky (cloudy) DRF for the BASE case and the experiments over land in summer. Since SSTs are prescribed and do not change relative to the BASE case, aerosol forcing affects the surface energy balance principally over land areas, hence our focus is on the land domains. The clear-sky aerosol SFC forcing over land (Table 2) is roughly a factor of 2 greater than the all-sky SFC DRF because clouds dominate the optical depth when present, causing aerosols to affect the surface primarily in cloud-free conditions [Erlick and Ramaswamy, 2003]. At the top of the atmosphere, with the exception of XChW, the all-sky anthropogenic DRF shifts in sign from negative to positive when comparing clear-sky with all-sky forcing, particularly for the HOD simulations. This is because strongly absorbing BC above highly reflective clouds has a stronger effect upon the planetary albedo compared to clear-sky conditions when the surface beneath the BC aerosol tends to be darker [Haywood and Ramaswamy, 1998].

[20] Unlike in the clear-sky case, the all-sky ratio of SFC forcing to TOA forcing is between -1 and -2 over India for all experiments except the most scattering experiment (XChW). The INDOEX field campaign SFC forcing was a factor of $+10$ larger than the TOA forcing in cloudy conditions [Ramanathan *et al.*, 2001b]. The difference between simulated and observed all-sky SFC and TOA forcing is not entirely surprising given that the modeled cloud distributions and aerosol vertical profiles used in the forcing calculation are different from those observed during the INDOEX study, which took place during a particular year over the northern Indian Ocean. The model results represent an average over time and the entire land domain. All-sky SFC, ATM, and TOA forcing from Menon *et al.* [2002] (-17 , $+23$, and $+6$ over India) are consistent with the forcings simulated for the absorbing HOD experiments as expected despite the fact that differences due to modeled cloud distributions are likely, especially for surface forcing. Compared to India, the all-sky SFC DRFs over China are

greater in part owing to the higher sulfate loadings and resulting higher optical depths in humid conditions, though BC and OC burdens are also higher over China. Since BC aerosols are effectively “white” in XChW, the ATM forcing is negligible.

[21] A more robust comparison between measured and modeled forcing can be made by normalizing the SFC, TOA and ATM clear-sky instantaneous direct radiative effect by the column-integrated aerosol extinction optical depth (τ_e) to obtain the clear-sky radiative efficiencies at the surface (β_s), at the top of the atmosphere (β_t), and in the atmosphere (β_a). The radiative efficiency is primarily dependent upon the single scattering albedo and the asymmetry factor (g) [Kim *et al.*, 2005]. In this sensitivity study, all experiments share the same asymmetry factors for BC and OC. However, the asymmetry factor changes as a function of model RH for sulfate (if sulfate is treated as hygroscopic).

[22] Table 3 presents the clear-sky shortwave total aerosol (natural plus anthropogenic) direct radiative efficiencies over India and China for each experiment as well as published estimates of β_s , β_t , and β_a from various field campaigns. Here we list forcing efficiencies for spring (MAM) over China (land and ocean average) and winter (DJF) over India (ocean only) to correspond more closely to the periods of the ACE-Asia [Clarke *et al.*, 2004] and INDOEX [Ramanathan *et al.*, 2001b] field campaigns, respectively. We also note that these modeled radiative efficiencies include the effects of both natural and anthropogenic aerosols in order to compare with observed estimates. As can be seen from Table 3, β_s for XCa falls within the INDOEX range of -70 to -75 W m^{-2} over the northern Indian Ocean within a polluted air mass. This is not surprising since the extinction optical depths used for this experiment were obtained from Collins *et al.* [2001] as described previously and optical depths during INDOEX ranged between 0.2 and 0.7 [Satheesh and Ramanathan, 2000] (DJF $\tau_e = 0.49$ over the ocean for XCa). Similarly, at the top of the atmosphere in clear-sky conditions, β_t from XCa is again closest to the INDOEX forcing efficiency of -22 W m^{-2} [Satheesh and Ramanathan, 2000; Ramanathan *et al.*, 2001b]. The ratio $\frac{\beta_s}{\beta_t}$ is an indication of absorption efficiency. With the exception of XChW, all experiments have $\frac{\beta_s}{\beta_t}$ close to the INDOEX observation. The more scattering simulation XChW has a lower ratio closer to the ratio of about 1.5 obtained when only scattering aerosols are present [Coakley and Cess, 1985; Haywood *et al.*, 1999]. The β_s over China in MAM for XCa lies within the range of observations, but the other HOD experiments tend to underestimate the magnitude of β_s . The difference between β_t and β_s yields the atmospheric radiative efficiency β_a . Kim *et al.* [2005] calculated atmospheric forcing efficiencies between $+39$ and $+67$ W m^{-2} per unit τ_e over east Asia using measurements from the Skyradiometer Network (SKYNET). The most absorbing simulation in the HOD regime (XCa) simulates β_a within the observed range.

[23] For India, XCa is overall the most representative of the surface, atmospheric, and TOA radiative efficiency in comparison to the observations. The other HOD experiments tend underestimate the magnitude of surface and atmospheric radiative efficiency over India, likely indicating that these experiments underestimate the proportion of absorbing aerosol. Over China, the surface and atmospheric

Table 3. June/July/August Clear-Sky Shortwave Aerosol Radiative Efficiency^a

| Experiment | β_s (SFC/ τ_e) | β_t (TOA/ τ_e) | $\frac{\beta_s}{\beta_t}$ | β_a (ATM/ τ_e) |
|---|----------------------------|----------------------------|---------------------------|----------------------------|
| <i>India^b</i> | | | | |
| LOD | | | | |
| XA | -48.3 | -21.4 | +2.3 | +26.9 |
| HOD | | | | |
| XCa | -71.4 | -20.3 | +3.5 | +51.1 |
| XCh | -49.4 | -20.3 | +2.4 | +29.1 |
| XChW | -28.0 | -29.8 | +0.9 | ≈ 0 |
| Observations | | | | |
| <i>Ramanathan et al.</i> [2001a, 2001b] | -70 to -75 | -22 | +3 | +48 to +58 |
| <i>Satheesh and Ramanathan</i> [2000] | | | | |
| <i>China^c</i> | | | | |
| LOD | | | | |
| XA | -39.0 | -20.2 | +1.9 | +18.8 |
| HOD | | | | |
| XCa | -67.2 | -10.7 | +6.3 | +56.5 |
| XCh | -39.1 | -15.2 | +2.6 | +23.9 |
| XChW | -24.0 | -24.2 | +1.0 | ≈ 0 |
| Observations | | | | |
| <i>Bush and Valero</i> [2003] | -74 | - | - | - |
| <i>Markowicz et al.</i> [2003] | -60 | - | - | - |
| <i>Conant et al.</i> [2003] | -55 | - | - | - |
| <i>Nakajima et al.</i> [2003] | -50 to -80 | -25 to -26 | +2 to +3 | +25 to +67 |
| <i>Kim et al.</i> [2005] | - | - | - | +39 to +67 |
| <i>Takamura et al.</i> [2007] | -81.6 | -32.5 | +2.5 | +49.4 |

^aUnit is $\text{W m}^{-2} \tau_e^{-1}$. All aerosol species (natural + anthropogenic) included in radiative efficiencies.

^bDJF values calculated over ocean only to match the time and spatial coverage of INDOEX more closely.

^cMAM values calculated over land and ocean to match the time and spatial coverage of ACE-Asia more closely.

forcing efficiency for XCa, the most absorbing case in the HOD regime, is comparable to the observations. However, the wide range of the observations makes a strict comparison difficult, and it is less clear which experiment best captures the observations of radiative efficiency over China. Even amongst the observations, there is a great deal of variability, pointing to the need for more constrained measurements.

4. Model Response

[24] As shown by *Chen and Ramaswamy* [1995] and *Erlick et al.* [2006], differing dynamical responses to the same solar forcing can be found in midlatitude versus tropical regions. Further, the climate and regional circulation patterns for India and China are dissimilar. Therefore, we have chosen to analyze the response of the GFDL AM2-LM2 GCM to the forcing described in section 3 over India and China separately. We concentrate in particular on the model's surface air temperature and hydrologic cycle response. We focus on the northern hemisphere summer months (JJA). A perturbation likely will not manifest itself in the annual mean if not statistically significant during these months [*Peixoto and Oort*, 1992; *Chen and Ramaswamy*, 1995; *Erlick et al.*, 2006]. Note that this does not mean that the aerosol effects on climate during the winter in this region are unimportant. Finally, for the HOD experiments, only one set of measurements was used to scale up τ_e [*Menon et al.*, 2002], and, as a result, these experiments exhibit no seasonality with respect to their anthropogenic aerosol mass distributions.

4.1. Simulated Response Over India

[25] Area-weighted average JJA land surface air temperature for the BASE case and the change in surface air

temperature between the experiments and the BASE case (ΔT_s) are shown in Table 4. Changes in surface air temperature with greater than 90% significance calculated using the student's t-test are printed in bold. The absorbing HOD experiments cause roughly the same amount of surface cooling over India even though XCa has an anthropogenic extinction optical depth roughly half that of XCh (Table 1). The decrease in ΔT_s for XChW is less than 0.2 K, similar to the surface temperature decrease found in the LOD simulation XA. Figure 2 shows the JJA spatial distribution of ΔT_s (grey shading indicates regions where ΔT_s is at or above the 90% confidence level). The mean observed climatological JJA surface air temperature change between the 1945–1955 decade and the 1985–1995 decade from the Climate Research Unit (CRU) of the University of East Anglia [*Brohan et al.*, 2006] is shown in Figure 2e. Note that the observations, unlike the model simulations, include the effects of GHG increases between 1950 and 1990, which would be nominally expected to produce a surface warming in most regions. The observations also include feedbacks associated with atmosphere-ocean interactions. In spite of any warming contributions that may have arisen owing to greenhouse gas increases, a slight surface cooling is apparent in regions of northern India and over much of China. The contrasts between the absorbing HOD and scattering HOD experiment (XChW) show the effects of aerosol absorption on surface air temperature change (Figure 2). Significant strong surface air warming is found over the Tibetan Plateau for the absorbing HOD experiments (XCa and XCh), which have relatively high $\Delta \tau_a$ in this high surface albedo region. Absorbing aerosols overlying highly reflective surface albedos exert a radiative warming tendency at the surface owing to multiple reflections between the surface and the absorbing aerosol layer

Table 4. June/July/August Surface Air Temperature and Lapse Rate Change Over Asia

| Experiment | ΔT_s^a (K) | Δ Lapse Rate ^b (K) |
|---|--------------------|--------------------------------------|
| <i>India BASE ($T_s = 297.42$ K)</i> | | |
| XA | -0.17 | -0.3 |
| XCa | -0.60 | -1.2 |
| XCh | -0.67 | -1.3 |
| XChW | -0.16 | +0.6 |
| <i>China BASE ($T_s = 290.26$ K)</i> | | |
| XA | -0.42 | -0.5 |
| XCa | -0.56 | -1.4 |
| XCh | -0.91 | -1.5 |
| XChW | -1.14 | 0.0 |

^aChange in surface air temperature is ΔT_s . Land-area average ΔT_s with $\geq 95\%$ confidence from student's t-test are indicated in bold.

^bLapse rate is calculated as the difference between the surface air temperature and the layer-average tropospheric temperature (T_{TT}), where T_{TT} is calculated following *Fu and Johanson* [2005]. Δ Lapse Rate is the difference between the lapse rate of the given experiment and the lapse rate of the BASE case. Positive numbers indicate decreased stability while negative numbers indicate increased stability relative to the BASE case.

[*Chylek and Coakley*, 1974]. Significant strong surface air cooling is found throughout the Indian Peninsula for XCa and XCh owing to decreased solar flux arising from increased τ_e and increased cloud amount (see Table 5). XChW indicates

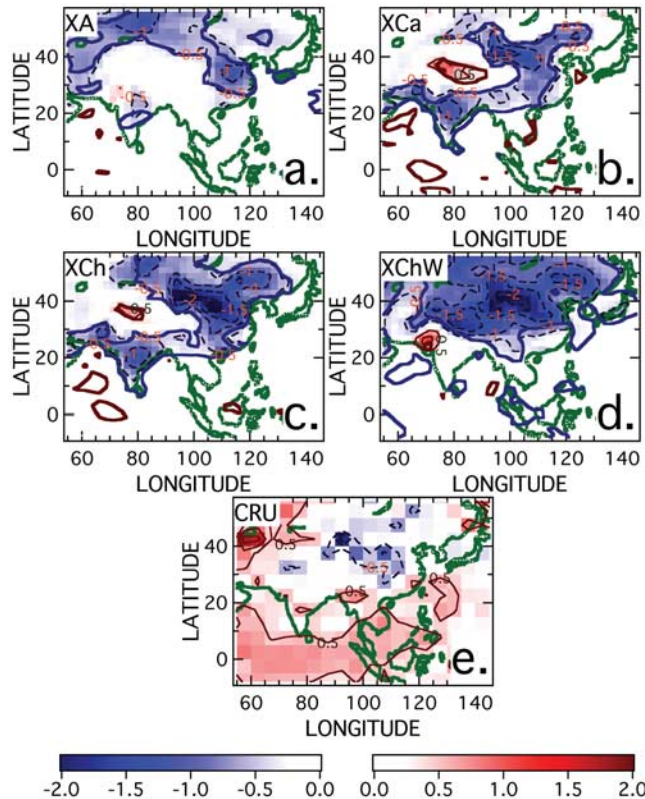


Figure 2. JJA change in surface air temperature (ΔT_s) (K) between the BASE case and (a) XA, (b) XCa, (c) XCh, and (d) XChW. (e) Observed mean ΔT_s between the 1945–1955 and 1985–1995 decades from the CRU database [Brohan et al., 2006]. Thin, solid (dashed) lines and red (blue) shading indicate positive (negative) ΔT_s (contour interval 0.5 K). Thick blue and red contours enclose regions where ΔT_s is at or above the 90% confidence level.

no significant change in surface air temperature over most of the Indian peninsula despite sharing aerosol extinction optical depth increases similar to XCh and a negative TOA DRF (Table 2). In XChW, reductions in cloud amount throughout India (Table 5) increase the amount of solar radiation reaching the surface, counteracting most of the surface solar flux reduction due to increased aerosol loading. Conversely, strong increases in cloud amount for the absorbing HOD experiments enhance the surface solar flux reduction. Both aerosols and clouds can contribute to a surface cooling tendency by reducing solar flux to the surface. Extinction due to all aerosol types, both absorbing and scattering, and clouds contribute to this so-called dimming. It should be noted that if GHG increases were considered in this study, the magnitude of the surface air cooling would be reduced, but warming signals, such as over central India in XChW, would likely increase.

[26] Figure 3 shows the zonally averaged JJA air temperature change (ΔT_{atm}) relative to the BASE case over India (averaged over $65^\circ E-90^\circ E$) and the increases in BC mixing ratio ($\mu g m^{-3}$) between 1950 and 1990. Figure 3 (color) also shows the change in shortwave all-sky heating rate ($K d^{-1}$) relative to the BASE case. In the HOD regime, the change in BC mixing ratio is the same for all experiments, but recall the BC is optically modeled as dry SO_4 in XChW. The similarity in atmospheric warming for experiments with nearly identical τ_a indicates that the atmospheric temperature is dependent on the ATM forcing (and the absorption optical thickness) when SSTs are prescribed [e.g., *Chung et al.*, 2002]. Atmospheric temperature changes over the Indian Ocean (south of $10^\circ N$) are generally small. Over the Indian Peninsula ($10^\circ N$ to $25^\circ N$) below 500 to 600 hPa, ΔT_{atm} and the shortwave heating rate decrease for the absorbing HOD experiments (XCa and XCh). This near-surface temperature cooling over land represents a transition between the surface cooling due to aerosol surface solar flux reduction and the atmospheric warming due to aerosol absorption aloft. This does not happen for the more scattering experiment XChW, as is to be expected.

Table 5. June/July/August Change in Cloud Amount Over Land^a

| Experiment | TOT | LOW | MID | HIGH |
|-------------------|------|------|------|-------|
| <i>India</i> | | | | |
| BASE ^b | 69.9 | 35.0 | 28.6 | 46.3 |
| XA ^c | 0.8 | 1.5 | 1.8 | -0.02 |
| XCa ^c | 2.4 | 3.4 | 5.2 | 1.7 |
| XCh ^c | 2.0 | 4.0 | 5.6 | 0.2 |
| XChW ^c | -6.4 | -4.4 | -1.6 | -4.8 |
| <i>China</i> | | | | |
| BASE ^b | 66.0 | 28.3 | 35.0 | 44.3 |
| XA ^c | 0.4 | 1.4 | 0.7 | -0.7 |
| XCa ^c | -0.2 | 2.5 | 0.8 | -0.7 |
| XCh ^c | 0.2 | 3.1 | 0.9 | -1.1 |
| XChW ^c | -1.7 | -1.2 | -0.6 | -2.5 |

^aChange given in percent. Cloud amount refers to the change in the spatially averaged frequency of occurrence of clouds [*Wetherald and Manabe*, 1988; *Erlick et al.*, 2006].

^bTotal (TOT), low-level (LOW), mid-level (MID), and high (HIGH) cloud regimes defined in text. Absolute cloud amount (%) given for BASE case.

^cChange relative to BASE case. Decreased cloud amount relative to BASE given in italics for clarity.

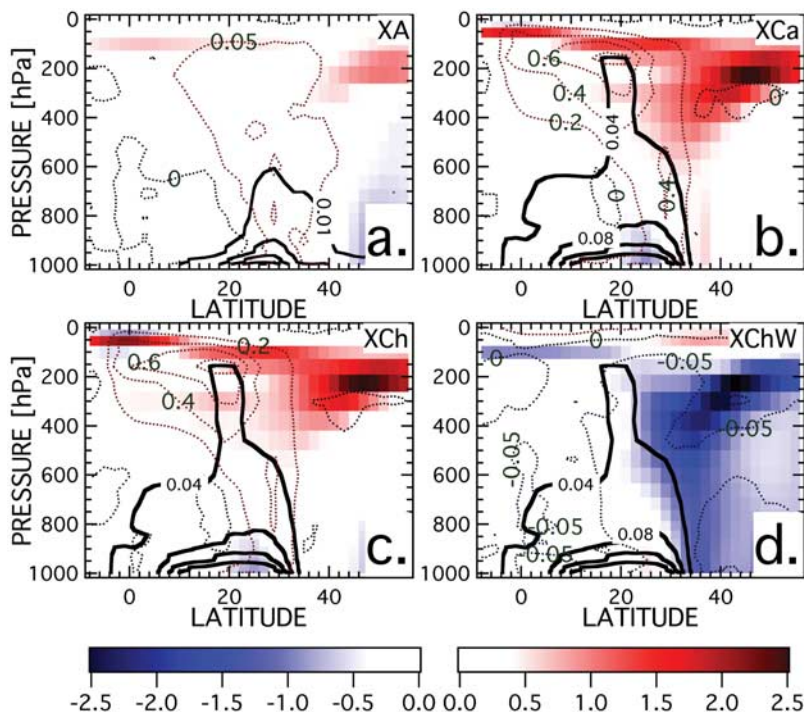


Figure 3. Zonally averaged change in JJA atmospheric temperature (ΔT_{atm}) (K) (shaded) over India ($65^{\circ}\text{E}-90^{\circ}\text{E}$) between the BASE case and (a) XA, (b) XCa, (c) XCh, and (d) XChW. Change in BC mixing ratio relative to the BASE case (thick black contours) with contour interval of 0.01 and $0.04 \mu\text{g m}^{-3}$ for XA and the HOD experiments, respectively. Thin, dotted contours indicate the change in shortwave heating rate (K d^{-1}) relative to the BASE case with contour interval of 0.05K d^{-1} for XA and XChW and 0.2K d^{-1} for XCa and XCh.

[27] We next examine the change in lapse rates over land arising in the various sensitivity studies (Table 4). We approximate the lapse rate as the surface temperature minus the layer-average tropospheric temperature, where the layer-average tropospheric temperature (T_{TT}) is derived from a linear combination of the simulated T2 and T4 microwave sounding unit (MSU) brightness temperatures following *Fu and Johanson* [2005]. These simulated brightness temperatures are calculated using the University of Alabama at Huntsville (UAH) MSU weighting functions, which have a near-zero contribution from the stratosphere. Since the lapse rate calculated in this manner is positive, a smaller lapse rate implies more stable conditions and a lesser tendency toward the vertical mixing of air [*Lazante et al.*, 2006]. Note that the change in lapse rate in Table 4 is with respect to the BASE case such that positive values (larger experimental lapse rates) indicate decreased stability and negative values (smaller experimental lapse rates) indicate increased stability compared to 1950. Surface cooling combined with warming aloft act to stabilize the column and decrease the change in lapse rate relative to the BASE case for all experiments except XChW. Over the Indian Peninsula (10°N to 25°N), ΔT_{atm} (Figure 3) slightly increases near the surface for XChW (owing to increased surface temperature) while the air aloft cools, resulting in a decrease in stability and an increase in the change in lapse rate. In the Tibetan Plateau region, strong, elevated heating from increased BC and sensible heating at the surface results in dry convection for XCa and XCh.

[28] Table 5 shows the area-averaged change in cloud amount relative to the BASE case over land. Note that “cloud amount” refers to the change in the spatially averaged frequency of occurrence of clouds [*Wetherald and Manabe*, 1988; *Erllick et al.*, 2006]. Low clouds are defined as those forming between 680 and 1000 hPa, middle clouds form between 440 and 680 hPa, and high clouds form between 10 and 440 hPa. Significant ($\geq 90\%$) increases in clouds occur over the ocean and coast lines of India in XCa and XCh. In XChW, significant decreases in clouds are observed over most of the Indian land mass, and clouds increase significantly over the Bay of Bengal ($\sim 8^{\circ}\text{N}-20^{\circ}\text{N}$, $80^{\circ}\text{E}-100^{\circ}$) for XA. Figure 4 shows the change in vertical velocity (pressure units) relative to the BASE case zonally averaged over India. Note that here we show $\Delta(-w)$ (or $\Delta\frac{-dp}{dt}$) such that positive values indicate increased upward motion and negative values indicate relative subsidence. All cloud types increase over land in the absorbing HOD simulations (despite the increase in atmospheric stability) owing to increases in vertical velocity at 20°N and 30°N (Figure 4). XA also exhibits increased cloud amount and increased vertical velocity near 20°N . The increase in vertical velocity represents an increased input of diabatic heating into the atmosphere which results in upward motion, particularly along the coast lines. Cloud amount decreases over land for the nonabsorbing HOD experiment XChW, and strong decreases in vertical velocity are seen north of 25°N (Figure 4), a striking mirror image and in sharp contrast to the absorbing HOD experiments.

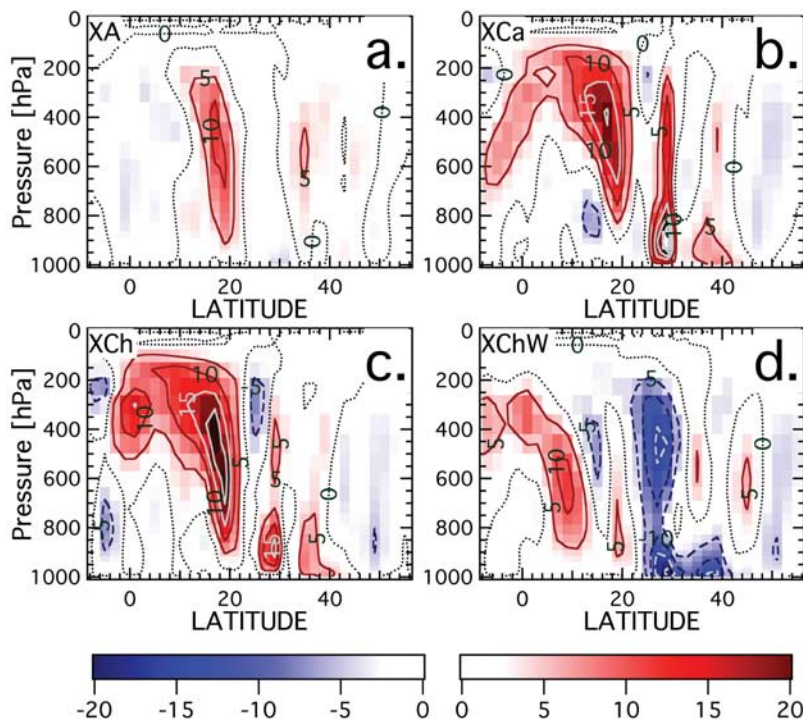


Figure 4. Zonally averaged JJA change in vertical velocity ($\Delta(-w) = \Delta\left(-\frac{dp}{dt}\right)$) between the BASE case and experiments over India ($65^{\circ}\text{E}–90^{\circ}\text{E}$) for (a) XA, (b) XCa, (c) XCh, and (d) XChW. Note that the negative of the vertical pressure velocity is taken such that red indicates increased vertical motion and blue indicates relative subsidence. The contour interval is $5 \times 10^{-5} \text{ hPa s}^{-1}$.

Note the strong increase in vertical velocity over the Tibetan Plateau ($\sim 30^{\circ}\text{N}$) in XCa and XCh, which is replaced with subsidence in XChW. Also note the strong increase in upward motion aloft over the Indian Ocean for the absorbing HOD experiments. The change in meridional circulation relative to the BASE case for the absorbing HOD experiments (not shown) indicates upward and northward advection of warm, moist air from over the ocean to the southern reaches of the Tibetan Plateau ($\sim 30^{\circ}\text{N}$). The above results exhibit the linkages between the semidirect effect, atmospheric heating, vertical velocity, and cloud amount.

[29] Figure 5 shows the change in surface pressure (ΔP_{sfc}) relative to the BASE case overlain with the change in 850-hPa winds relative to the BASE case (vectors), with gray shading indicating the 90% significance of ΔP_{sfc} . For XCa, ΔP_{sfc} decreases west of about 75°E and in the Tibetan Plateau region. In this simulation, ΔP_{sfc} increases slightly over most of eastern India and the Bay of Bengal. The change in 850-hPa winds advects air from over the ocean into northwestern India, with increased convergence leading to relatively strong increases in vertical velocity around 20°N (Figure 4). The wind change shifts to a more westerly direction over the southern reaches of the Tibetan Plateau and the northernmost part of the Bay of Bengal, resulting in strong convergence and upward motion in this region. The wind change pattern is similar for XCh. The pattern of ΔP_{sfc} for XA is similar to the absorbing HOD experiments; however, the 850-hPa wind changes are slightly different, and the wind changes are generally southwesterly over the Arabian Sea and then traverse the Indian Peninsula in a westerly direction, again becoming southwesterly along the

eastern coast of India and throughout the Bay of Bengal. It is also interesting to note that the dipole pattern in ΔP_{sfc} for XA, XCa, and XCh is qualitatively consistent with the results of *Lau et al.* [2006]. For the nonabsorbing HOD experiment XChW, ΔP_{sfc} increases over northwest India and decreases over most of the ocean. The dipole pattern of ΔP_{sfc} reverses and the change in 850-hPa winds reverses direction compared to the absorbing HOD simulations, which results in divergence and subsidence along the western coast of India and the northern part of the Bay of Bengal. The change in circulation arising from the significant changes in surface pressure enhance the regional BASE case monsoon circulation in XCa and XCh and oppose it in XChW, indicating that at the high optical depths considered here, the model's regional circulation is sensitive to the amount of absorbing aerosol (i.e., τ_a). Thus, large-scale convergence is coupled to the aforementioned changes in the semidirect effect, diabatic heating, and cloud amounts.

[30] Evaporation (not shown) decreases over the land and increases slightly over most of the northern Indian Ocean ($\sim 8^{\circ}\text{S}–10^{\circ}\text{N}$, $55^{\circ}\text{E}–100^{\circ}\text{E}$) relative to the BASE case owing to increases in wind speed. However, for XCa extending from the Bay of Bengal eastward over southeast Asia, (and to a lesser extent for XCh) there is a region of decreased evaporation corresponding to the region of strong divergence and the increase in ΔP_{sfc} from Figure 5. In this same region, XChW has a region of increased evaporation corresponding to the region of strong increased convergence and decreased ΔP_{sfc} . This also corresponds to the southward shift of the westerly 850-hPa change in winds in

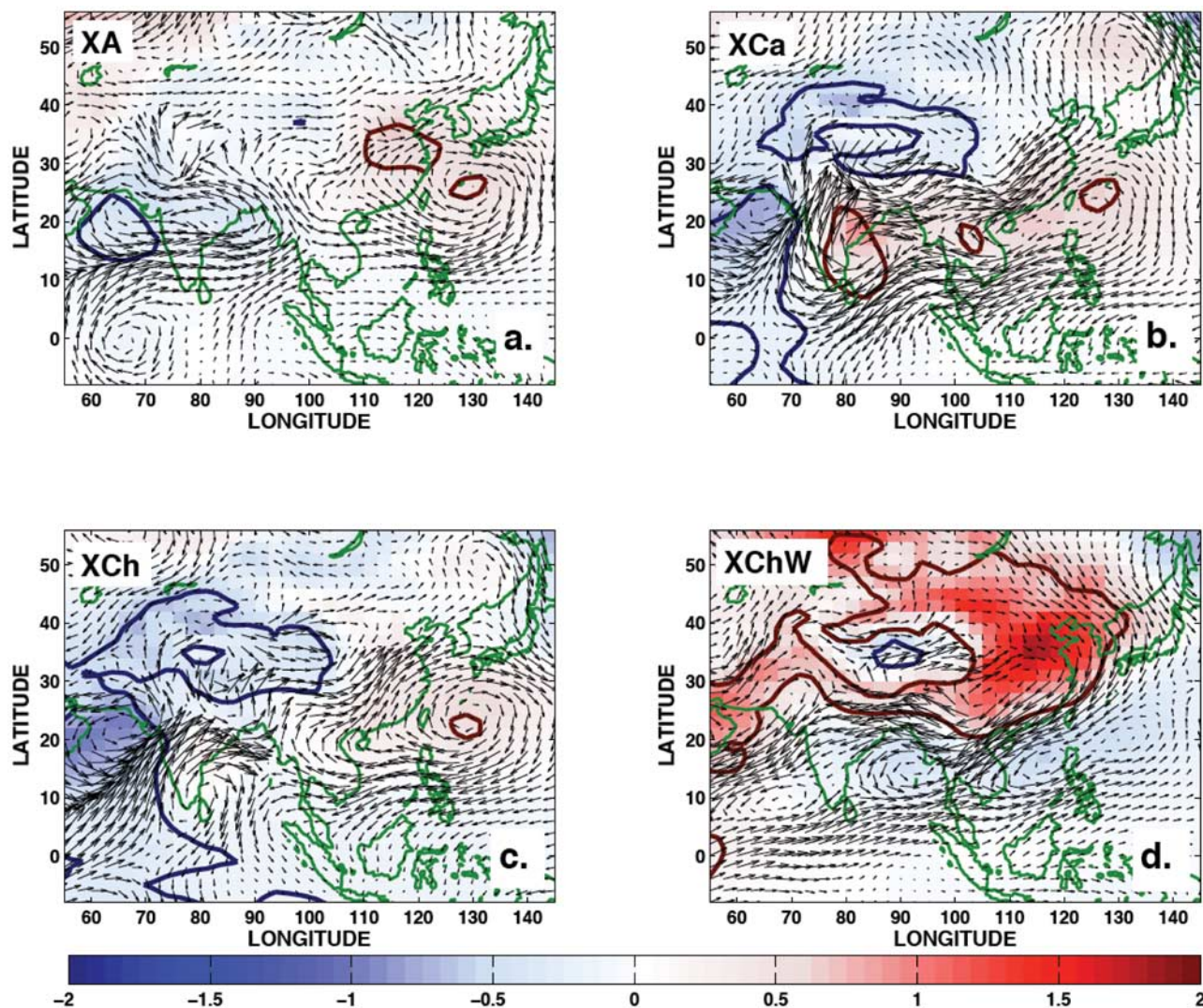


Figure 5. Change in JJA surface pressure (ΔP_{sfc}) (hPa) relative to the BASE case (shaded) for (a) XA, (b) XCa, (c) XCh, and (d) XChW. Thick blue and red contours enclose regions where ΔP_{sfc} is at or above the 90% confidence level. Changes in the 850-hPa winds relative to the BASE case are plotted as vectors.

Figure 5. In experiments with increased absorption (XCa and XChW), there is generally an increase in column-integrated water vapor over the land in India (not shown). In contrast, in the scattering XChW experiment, there is a decrease in precipitable water vapor, particularly in northern and northwestern India. There is a similarity in the spatial pattern of column-integrated water vapor and the layer-averaged tropospheric temperature. Generally, tropospheric warming due to increased aerosol absorption is accompanied by increased column-integrated water vapor, and tropospheric cooling associated with increases in only scattering aerosols is accompanied by decreased precipitable water.

[31] The spatial distribution of the change in precipitation rate relative to the BASE case (ΔP) shown in Figure 6 reveals increases in precipitation corresponding to regions of convergence and increased vertical motion, and decreases in precipitation corresponding to regions of divergence and relative subsidence. LOD regime (XA) changes in precipitation are generally not significant (grey shading indicates 90% confidence level). Precipitation changes for the two absorb-

ing HOD experiments (XCa and XCh) are almost similar to each other over India. For the absorbing HOD experiments, significant increases in precipitation occur over the northernmost region of the Bay of Bengal, and both experiments show significant increases in precipitation along the northwestern coast of India. Strong decreases in precipitation over most of the central Indian subcontinent are seen in all HOD experiments. We note that the ΔP pattern observed for XCa and XCh over India is qualitatively similar to the results of Menon *et al.* [2002] for an experiment similar to XCa. Also note that the strong decreases in precipitation simulated over the southern Bay of Bengal and stretching eastward in XCa and XCh are replaced by strong increases in ΔP in this same region for XChW, corresponding to changes in ΔP_{sfc} from Figure 5. The differences in the precipitation anomaly spatial distributions between the absorbing HOD experiments and XChW imply that the imposed aerosol forcing can, depending on the scattering and absorbing aerosol proportions, influence and even reverse the precipitation pattern in south and east Asia relative to the control case.

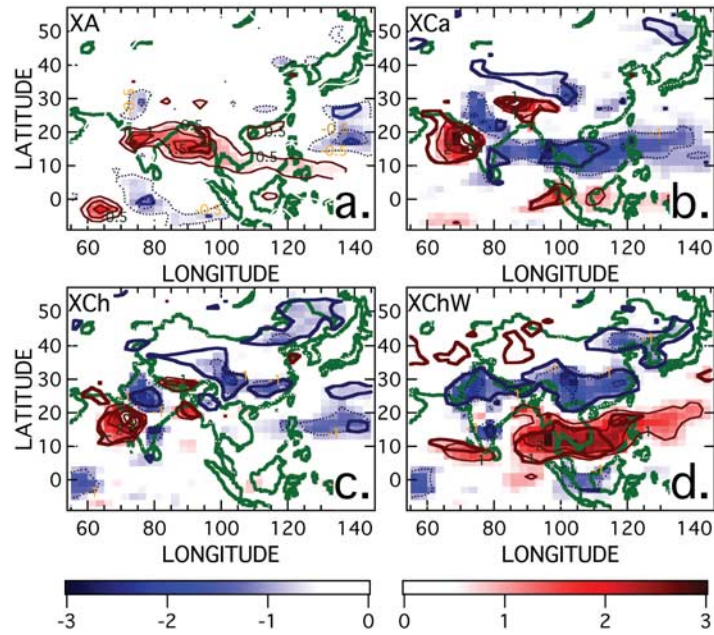


Figure 6. Change in JJA precipitation rate (ΔP) relative to the BASE case for (a) XA, (b) XCa, (c) XCh, and (d) XChW. Thin, solid (dotted) contours and red (blue) shading indicate positive (negative) ΔP (contour interval of 0.5 and 1 mm d^{-1} for XA and the HOD experiments, respectively). Thick red and blue contours inclose regions where ΔP is at or above the 90% confidence level.

[32] Following the hypothesis of *Chung et al.* [2002], the initial surface and atmospheric forcing imposed by the absorbing 1990 aerosols serve to decrease the temperature contrast in the north-south direction in the low-level atmosphere as the land air surface temperature cools and the air over the oceans warms relative to the ocean surface (where surface temperature does not change because of prescribed SSTs). This leads to an increase in the 850-hPa winds, strengthening the mean monsoon circulation of the BASE case and increasing convergence and evaporation over the ocean and along the western coast of India. In turn, vertical velocity is increased, leading to increases in clouds and precipitation in this region. Increased clouds resulting from increased vertical velocities further decrease solar flux to the surface, enhancing surface cooling and low-level convergence, thus producing a positive feedback. Over land, increased temperature aloft and surface cooling increases stability, inhibits convection, decreases evaporation, and increases relative humidity [*Ramanathan et al.*, 2005]. Relative humidity (not shown) increases in the absorbing HOD experiments but decreases over land in the most scattering experiment (XChW).

[33] Strong negative aerosol surface forcing in XChW also serves to decrease the north-south temperature gradient. However, the increase in scattering aerosol only does not increase atmospheric heating and upward motion, and the resulting decrease in cloud amount increases the solar flux to the surface. The surface energy budget reveals the importance of aerosol extinction versus cloud changes in determining the net shortwave flux to the surface. In the global annual mean, the surface energy budget is given by

$$S + F + LE + H \approx 0, \quad (1)$$

where the net (down minus up) solar (shortwave) heat flux at the surface is denoted by S , the net infrared (longwave) surface heat flux is F , and LE and H are the net latent and sensible heat fluxes at the surface, respectively. The sign convention is such that positive terms warm the surface and negative terms cool the surface. Oceanic transport of heat is not considered since SSTs are prescribed. Note that the fluxes in this equation are taken after equilibrium has been reached; they are not instantaneous fluxes and thus reflect the energy balance at the surface after feedbacks (e.g., clouds) have occurred. Equation (1) can be rewritten following *Boer* [1993] and *Chen and Ramaswamy* [1996] as

$$\begin{aligned} (S_0 - \sigma T_{sfc}^4) + (G_{clr} + W_{clr}) \\ + (C_{SW} + C_{LW}) + A_{sfc} + LE + H \approx 0, \quad (2) \end{aligned}$$

where S_0 is the global annual-mean solar radiation incident at the top of the atmosphere; σT_{sfc}^4 is the blackbody surface emission; G_{clr} is the downward longwave emission by the clear-sky atmosphere; W_{clr} represents the solar radiation absorbed in the clear-sky atmosphere owing to absorption and scattering by gas molecules and aerosols; C_{LW} and C_{SW} are the longwave and shortwave surface cloud forcings; and A_{sfc} is the radiative effect due to the surface albedo.

[34] Table 6 shows the value for each of the terms in equation (1) for the BASE case and the change in each term in equation (2) relative to the BASE case for each experiment. Again note that all quantities are evaluated at equilibrium, i.e., after adjustments have occurred in response to the imposed experimental aerosol perturbations. For the BASE case, the net effect of solar flux input is, as expected, to warm the surface, while latent, sensible, and net longwave fluxes act to cool the surface. Using equation (2) to analyze surface

Table 6. June/July/August Land Surface Energy Balance^a

| | Shortwave (S) ^b | | | Longwave (F) ^c | | | Latent (LE) | Sensible (H) |
|------------|--------------------------------|----------|-----------|-------------------------------|----------|---------------|-----------------|------------------|
| | W_{clr} | C_{SW} | A_{SFC} | G_{clr} | C_{LW} | $-\sigma T^4$ | | |
| | | | | <i>India</i> | | | | |
| BASE | | 167.6 | | | -47.1 | | -79.5 | -36.6 |
| LOD Change | | | | | | | | |
| XA | -9.6 | -0.5 | 1.9 | 0.2 | 0.4 | 1.6 | 2.8 | 3.1 |
| HOD Change | | | | | | | | |
| XCa | -38.9 | 0.1 | 7.3 | -1.0 | 1.3 | 5.9 | 16.0 | 9.7 |
| XCh | -50.6 | 8.3 | 7.9 | -0.8 | 0.9 | 6.4 | 18.0 | 10.4 |
| XChW | -25.2 | 27.2 | -1.0 | -3.7 | -2.2 | -0.7 | 7.4 | -3.5 |
| | | | | <i>China</i> | | | | |
| BASE | | 187.1 | | | | -85.4 | -35.8 | |
| LOD Change | | | | | | | | |
| XA | -14.6 | 4.6 | 1.8 | -1.6 | 0.2 | 3.1 | 3.6 | 2.9 |
| HOD Change | | | | | | | | |
| XCa | -44.0 | 10.3 | 6.1 | -0.7 | 0.3 | 5.7 | 12.7 | 10.1 |
| XCh | -59.4 | 20.7 | 7.0 | -1.3 | -0.6 | 7.8 | 16.0 | 10.3 |
| XChW | -34.5 | 24.9 | 1.3 | -5.1 | -1.8 | 7.1 | 4.4 | 1.9 |

^aGiven in $W m^{-2}$. Base case follows equation (1) and uses absolute values; experiments are change in parameters from equation (2) relative to BASE case. Negative values (cooling or less warming) are given in italics for clarity. Note that energy balance closure is not obtained for JJA but is obtained in the annual mean (not shown).

^b $S = S_0 + W_{clr} + C_{SW} + A_{SFC}$; see text for definitions of S_0 , W_{clr} , C_{SW} , and A_{SFC} . Note S_0 does not change between the BASE case and experiments.

^c $F = G_{clr} + C_{LW} - \sigma T^4$; see text for definitions of G_{clr} , C_{LW} , and σT^4 .

energy changes over India, we see that the largest cooling arises from changes in δW_{clr} , with the magnitude of the decrease related primarily to $\Delta\tau_e$ (Table 1). C_{SW} is calculated as the difference between the all-sky downward shortwave flux and the clear-sky downward shortwave flux [Erlick and Ramaswamy, 2003]. Thus, despite the large increases in cloud amount in XCa and XCh (and thus large decreases in all-sky downward solar flux), the larger magnitude of the decrease in downward clear-sky solar flux owing to the large $\Delta\tau_e$ leads to a positive δC_{SW} (i.e., a warming tendency). However, the cooling from δW_{clr} is larger in magnitude than the δC_{SW} warming for these experiments. Cloud amounts increase in XA, but the aerosol extinction optical depth is not high enough to cause a positive δC_{SW} (warming) as in the absorbing HOD simulations. Strong cloud amount decreases for XChW makes shortwave cloud-forcing the leading warming term from equation (2), and greater in magnitude than the cooling due to δW_{clr} .

[35] Net downward longwave radiation is increased for XA, XCa, and XCh owing to the combined effects of changes in (1) downward longwave emission from increased water vapor, (2) downward longwave radiation from increased atmospheric temperature (Figure 3), and (3) longwave emission from increased clouds (Table 5) [Ramaswamy and Kiehl, 1985]. Decreases in upward longwave emission from the cooler surface imply a lesser cooling effect and contribute to a positive δF for these experiments. Changes in blackbody surface cooling follow logically from changes in surface air temperature (Table 4), with little change for XChW in the area-averaged sense. Relative blackbody surface warming occurs for the other simulations because the decreased surface temperature emits less blackbody radiation. Changes in clouds, particularly increases in high clouds, for XA, XCa, and XCh, contribute to warming due to longwave cloud forcing (δC_{LW}), and contribute to decreases in C_{LW} (cooling) for XChW. Decreased evaporation over land in India for all experiments agrees with the decreased latent cooling (increased latent warming) for all experiments. The change

in sensible heating warms the surface (cools the surface less) for all experiments (except XChW), indicating an increase in stability as surface temperatures cool and temperatures aloft warm in accord with the changes in lapse rates from Table 4. In the HOD regime, stability increases over land substantially when absorbing aerosols are present.

[36] There is a remarkable similarity in the air temperature and hydrologic cycle response of the model to high absorption optical depth increases even if scattering and extinction optical depths are very different (XCa and XCh). The atmospheric temperature response reflects the prominent influence of the absorption optical depth. With large increases in τ_e , the surface temperature response and the response of the hydrologic cycle are sensitive to $\Delta\tau_a$. For smaller changes in τ_e (LOD regime), the response of the model's hydrologic cycle is not as significant for the changes in aerosol optical properties considered in this study. This fact makes it difficult to discriminate between the LOD cases with the same $\Delta\tau_a$ (XBa and XBh; see Table 1 and auxiliary material). Recall that $\Delta\tau_e$ for XCh and XChW is expected to be an overestimate compared to reality. Similarly, ω_o for XChW represents unrealistically high scattering for 1990 aerosols over this region. Given that the aerosol optical properties and forcing efficiencies from sections 2.2 and 3 for XCa are consistent with observations over India, and that the surface air temperature response for XCa is qualitatively consistent with observations, this experiment seems most representative of the anthropogenic aerosols over India.

4.2. Simulated Response Over China

[37] Area-averaged surface air temperature decreases over China with greater than 90% significance for all HOD experiments (Table 4). The magnitude of ΔT_s increases with the magnitude of SFC forcing; however, aerosol radiative forcing should not be viewed as the sole contributor to this decrease in surface air temperature.

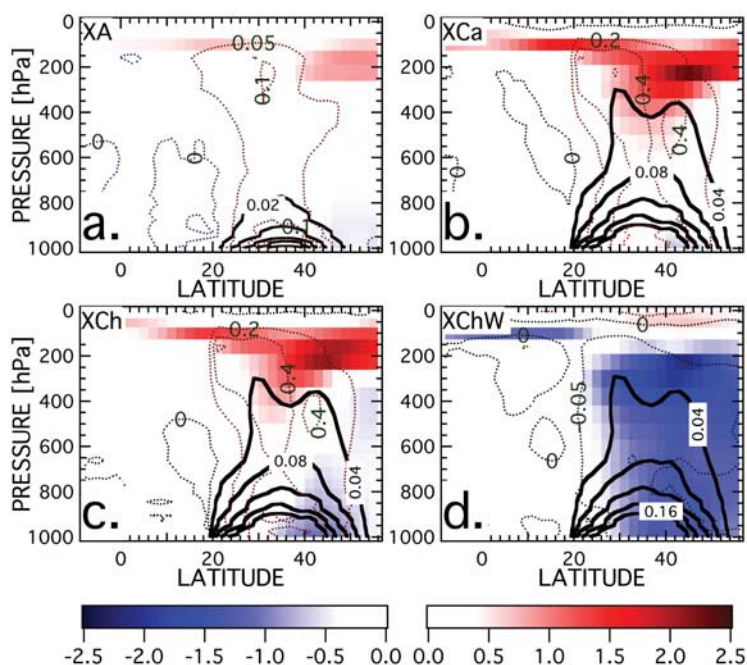


Figure 7. Same as Figure 3 (color version; ΔT_{atm} , BC mixing ratio change, and shortwave heating rate change) except zonally averaged over China (90°E – 130°E).

Though the magnitude of the surface air temperature decreases in the HOD regime are large compared to observations (Figure 2e), it is important to note that anticipated warming associated with increased GHGs in the twentieth century would reduce the cooling in XCa and XCh, likely bringing them closer to observations over large portions of China. ΔT_s decreases with greater than 90% significance over most or all of China for the HOD simulations (Figure 2). The greatest cooling occurs in the north-central part of China coincident with the greatest $\Delta \tau_e$ (Figure 1). The surface air cooling pattern for the absorbing HOD experiments over China is qualitatively similar to the observed surface air temperature cooling in Figure 2e, which is particularly interesting since it contrasts sharply with the general warming trend of surface temperature associated with long-lived GHG increases [Solomon *et al.*, 2007]. Unlike the scattering HOD experiment (XChW), which shows cooling throughout China and over the Tibetan Plateau, the absorbing HOD experiments have cooling over eastern China with reduced cooling or warming over Tibet consistent with the observations.

[38] Figure 7 shows ΔT_{atm} and the change in BC mixing ratio ($\mu\text{g m}^{-3}$) relative to the BASE case zonally averaged over China (90°E – 130°E). The change in zonally averaged shortwave heating rate (K d^{-1}) relative to the BASE case is shown in Figure 7 (color). There is little change in atmospheric temperature and shortwave heating rate south of the region of increased BC in China (south of 20°N). Lower-level cooling is found over most of China with strong warming aloft. Note that the strong warming in the region of the midlatitude jet stream, which originates in part as warming over the Tibetan Plateau region, is apparent with a smaller magnitude in the global mean (not shown). This is due to the strong zonal winds at this altitude, which tend to advect the anomaly induced by the radiative heating around

the globe. XChW indicates cooling throughout the troposphere over China. Warming at higher altitudes combined with surface cooling (Figure 7) causes stabilization of the troposphere and a decrease in the lapse rate over land relative to the BASE case for all experiments except XChW (Table 4).

[39] From Table 5, area-average low- and mid-level clouds generally increase in the model over China for XA, XCa, and XCh. All cloud types decrease for XChW. For the absorbing HOD simulations, all cloud types increase strongly in northeastern China and in a band between 20°N and 30°N stretching from northern India eastward through China, with a corresponding strong decrease in cloud amount in a band to the south between 10°N and 20°N (not shown). In contrast, the nonabsorbing HOD simulation (XChW) exhibits strong decreases in all cloud types between 20°N and 30°N and strong increases between 10°N and 20°N . The contrast in cloud changes between the absorbing HOD experiments and XChW is another indicator of contrasts effected on circulation if only pure scattering aerosol increases are considered.

[40] The changes in cloud amount are related to the change in vertical pressure velocity ($\Delta(-w)$) zonally averaged over China in Figure 8. In the HOD regime for absorbing aerosol, there is strong subsidence over the ocean between 10°N and 20°N with rising motion to the north over the land between 20°N and 30°N . This pattern of vertical velocity change is reversed for XChW. It is interesting to note that the change in vertical pressure velocity for XCa is qualitatively consistent with the results of Menon *et al.* [2002]. Increasing the scattering optical depth while holding the absorption optical depth constant (XCh) tends to weaken the magnitude of these changes in vertical motion (also exhibited in XBa and XBh; see auxiliary material), indicating the important roles played by both scattering and

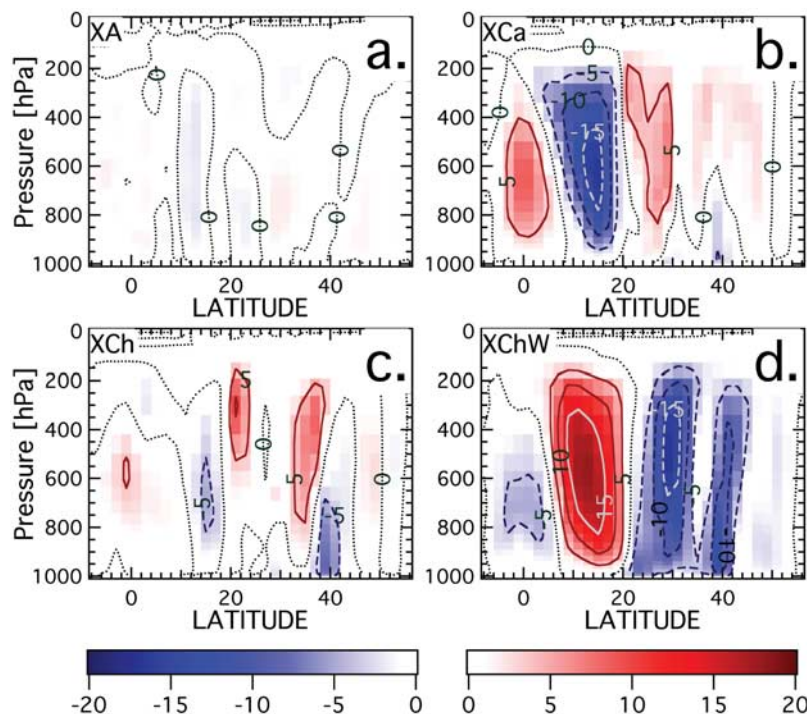


Figure 8. Same as Figure 4 (color version; $\Delta(-w) = \Delta \frac{-dp}{dt}$; contour interval $5 \times 10^{-5} \text{ hPa s}^{-1}$) except zonally averaged over China (90°E – 130°E).

absorbing components of anthropogenic aerosols, and the striking contrast when only scattering aerosols are considered (XChW).

[41] As was the case over India, changes in vertical velocity and cloud amount are related to changes in low-level convergence associated with the changes in circulation and surface pressure in Figure 5. The ΔP_{sfc} increase in XA, XCa, and XCh is centered off the southeastern coast of China in the East China Sea. This high extends southwestward from the East China Sea, over all of Southeast Asia, and into the Bay of Bengal and eastern India for XCa. The circulation change results in strong low-level convergence (not shown), increased upward motion (Figure 8), and increased cloud amount (Table 5) over most of southern and eastern China (particularly for XCa) between 20°N and 30°N with strong divergence, subsidence, and decreased cloud amount to the south between 10°N and 20°N . In XCa, warm, moist air from over the ocean is advected into southern and eastern China, while in XCh air from over the ocean is advected into northeastern China. In the nonabsorbing HOD experiment (XChW), the spatial pattern of ΔP_{sfc} is reversed relative to the absorbing HOD experiments, with strong increases in ΔP_{sfc} over the land in China and decreased ΔP_{sfc} to the south between 10°N and 20°N . The pattern of the change in 850-hPa winds relative to the BASE case reverses, and northeasterly winds advect cold, dry air from the north over southeastern China and into the northern reaches of the Bay of Bengal, opposing the monsoon circulation of the BASE case. Strong convergence is accompanied by cloud amount increases between 10°N and 20°N with divergence and strong cloud amount decreases to the north between 20°N and 30°N , corresponding to the strong

decrease and increase, respectively, in upward motion from Figure 8.

[42] Evaporation over China (not shown) decreases relative to the BASE case everywhere over land for all experiments, with the strongest decreases associated with the absorbing HOD experiments. Over the ocean to the east of mainland China, XChW indicates increased evaporation not seen in the other experiments. Precipitable water (not shown) increases over northeastern China in the LOD experiments and decreases in southeastern China. In the HOD regime, column-integrated water vapor increases over China for the absorbing experiments and strongly decreases for the nonabsorbing experiment XChW.

[43] In the HOD regime, precipitation (Figure 6) generally decreases over most of China, but these decreases are significant only in parts of central, southeastern, and northeastern China, particularly for XCh and XChW. This may, as suggested by *Gu et al.* [2006], indicate that precipitation in this region is more dependent on τ_e than τ_a ; however, we do not rule out the possibility that nonlocal changes in aerosols and clouds may alter the precipitation in southern China. There is a significant, strong decrease in ΔP between 10°N and 20°N in XCa while ΔP increases in this same region for XChW. Though XCa has similar changes in vertical velocity to *Menon et al.* [2002], it does not indicate the strong increases in precipitation over eastern and southern China reported by *Menon et al.* [2002] and observed as flooding in the Yangtze River valley (around 30°N – 32°N). The region of strongly decreased precipitation between 10°N and 20°N in XCa (Figure 6), however, is qualitatively consistent with the results of *Menon et al.* [2002]. For an experiment similar to XChW (i.e., increases in scattering aerosols only) but with $\Delta\tau_e$ comparable to XCa, *Menon et*

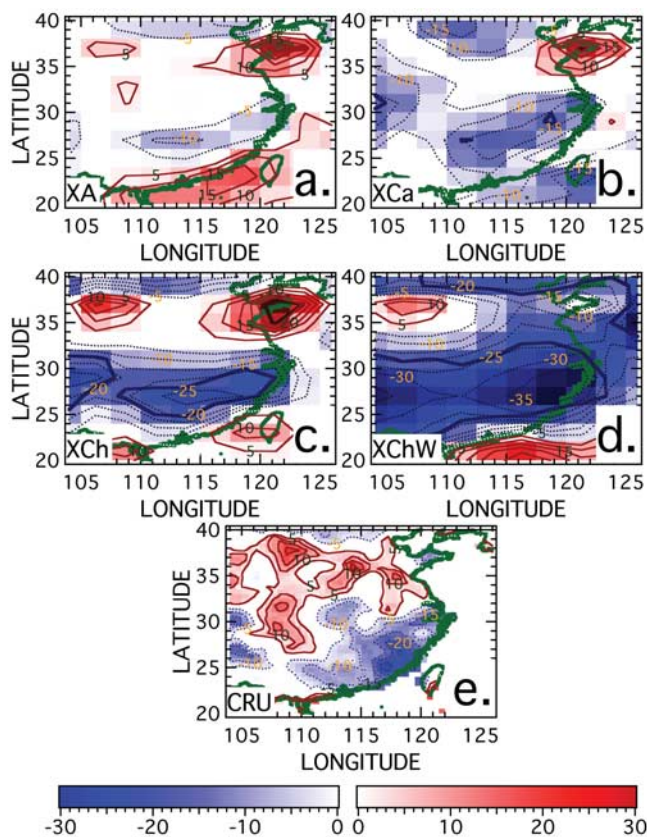


Figure 9. Percent change in total precipitation rate relative to the BASE case ($(\text{EXP} - \text{BASE})/\text{BASE} \times 100$) over China for: (a) XA, (b) XCa, (c) XCh, and (d) XChW. (e) Observed percent change in total precipitation between the 1985–1995 decade and the 1945–1955 decade from the CRU database [Brohan *et al.*, 2006]. Solid (dotted) contours and red (blue) shading indicate increased (decreased) precipitation (5% contour interval). Thick blue and red contours enclose regions where the change in precipitation is at or above the 90% confidence level.

al. [2002] did not simulate the strong increases in precipitation seen between 10°N and 20°N , suggesting intermodel differences in the precipitation response to aerosol perturbations. Given that model physics (e.g., convection, cloud microphysics and optics, boundary layer) differ, it is not surprising to find such intermodel differences.

[44] Observations indicate a trend toward increased drought in a region of southeast China (23°N – 27°N , 114°E – 120°E) [Cheng *et al.*, 2005]. Figure 9 shows the percent change in precipitation relative to the BASE case for southern China (grey shading indicates 90% confidence level). Figure 9e shows the observations from the CRU precipitation data set [Brohan *et al.*, 2006]. Relative to the observations, all experiments except XChW capture some increased rainfall in the region of the Yangtze River Basin ($\sim 30^{\circ}\text{N}$ – 32°N , 114°E – 120°E) and decreased rainfall in the southeastern drought region, indicating a distinctive regional influence that anthropogenic aerosols have likely exerted over the past few decades. It is possible that the strong aerosol-induced signature seen in the HOD simulations

could be significantly offset when effects due to simultaneous greenhouse gas increases are also considered.

[45] Cheng *et al.* [2005] investigated the effects of the aerosol indirect effect and increased SSTs on precipitation in southern China using the ECHAM4 GCM. They concluded that the flooding region over the Yangtze River Basin in eastern China is more likely controlled by strengthened convective precipitation associated with SST increases (caused by GHG warming) which increase the strength of the Western Pacific Subtropical High (WPSH), the high-pressure system that controls the distribution of rainfall in southern and eastern China. They note, however, that both increases in aerosols and changes in SSTs (due to increases in GHGs) contribute to an increase in low cloud cover (via the indirect aerosol effect) and a decrease in precipitation over the drought region. In our simulations (which do not include indirect aerosol effects), low-level cloud cover increases over southeastern China for all absorbing HOD experiments and XA.

[46] Since SSTs were prescribed in the experiments, the similarity between the simulated change in precipitation and the observations in both the flooding region (Yangtze River basin) and the drought region cannot be attributed in this study to be due to SST anomalies. Since all the experiments capture the observed precipitation pattern to some extent qualitatively, it is difficult to ascribe this apparent similarity to the increase in absorbing aerosols. We note, however, that at higher optical depths when some absorbing aerosol is present (particularly XCh), we find significant decreases in precipitation in the southeastern drought region and increases (though not significant ones) to the north similar to the observations whereas the scattering XChW experiment does not simulate increased precipitation in the northeast. Similar to the findings of Huang *et al.* [2007] we also observe east-west “bands” of alternating sign of precipitation change (Figure 6; e.g., between 10°N and 20°N and between 20°N and 30°N in XCa and XCh). These bands, which correspond to regions of increased and decreased vertical motion (Figure 8), may affect the rate of appearance and retreat of the monsoon rains over China [Huang *et al.*, 2007]. For all experiments over China (except XChW), the low-level pressure increase in northeastern China acts as an extension of the western Pacific subtropical high (WPSH), moving the Meiyu rain belt in China northward and northwestward inland (over the Yangtze River valley) and in effect weakening the east Asian monsoon [Chang *et al.*, 2000; Lau *et al.*, 2006] and contributing to increased convergence, upward motion, and rainfall in this region ($\sim 30^{\circ}\text{N}$). Thus, from the simulations, it is apparent that at least some amount of absorbing anthropogenic aerosol is necessary to capture the spatial pattern of precipitation changes and thus be qualitatively consistent with the observations.

[47] Equation (1) and Table 6 indicate that $L\delta E$ is the dominant warming term as evaporation decreases over the land surface in China. XCh has the largest overall decrease in net shortwave radiation at the surface due to its high τ_e , high τ_a , and overall increase in cloud amount. XChW shows a much weaker decrease in surface dimming (δS) because of strong decreases in cloudiness (Table 5). δH is positive for all experiments, indicating an increase in stability; however it is $< 2 \text{ W m}^{-2}$ for XChW, which shows

little change in stability (Table 4). It is interesting to note that δH is positive for XChW over China and negative for this same experiment over India. This is due to decreased tropospheric stability in XChW over India and little change in stability over China (Table 4).

[48] The δW_{clr} is again the leading cooling term over China in equation (2). XCh has the greatest δW_{clr} cooling owing to its large τ_e . XCa has a similarly large δW_{clr} cooling compared to XCh despite having half the extinction optical depth because XCa is more absorbing than XCh. XChW has a smaller δW_{clr} compared to its absorbing counterparts. δC_{SW} is warming for all experiments, despite increases in low- and mid-level clouds (Table 5) since the change in clear-sky downward flux is more negative than the (negative) change in all-sky downward flux. Again, changes in blackbody surface cooling follow from the surface temperature decreases (Table 4), with the most warming (least cooling) resulting for XCh. The δC_{LW} is small for all experiments in agreement with small changes in cloud amount, particularly with small changes in high cloud amount (Table 5).

5. Discussion

[49] By considering a range of aerosol extinction optical depths and a range of aerosol absorption optical depths guided by the available observations of τ_e and ω_o , this study has been able to arrive at a more comprehensive picture of the possible climate response to anthropogenic aerosols (consisting of scattering and absorbing components) under conditions of prescribed SSTs. The results of this study indicate that the combined direct and semidirect effects of anthropogenic aerosols may have contributed to a portion of the observed changes in surface air temperature and precipitation between 1950 and 1990. In particular, this study shows that aerosol influences on the hydrologic cycle are sensitive to the amount of absorbing aerosol (τ_a). Increased absorbing aerosols over the region of south and east Asia, which includes the Tibetan Plateau, contribute to an enhancement of the monsoon circulation of the control case and thus influence changes in low-level convergence, vertical motion, cloud amount, and precipitation (statistically significant at high optical depths). Purely scattering aerosols, on the other hand, counteract the BASE case monsoon circulation and lead to opposite changes in cloud amount and precipitation. The intensification (weakening) of the monsoon circulation due to heating (cooling) over the Tibetan Plateau is consistent with recent observational evidence built upon a 2000-year time series of the Tibetan Plateau surface temperature based upon five surface air temperature reconstructions [Feng and Hu, 2005]. Recent analysis of satellite and reanalysis data also supports the relationship between aerosol heating over the Tibetan Plateau and an enhanced monsoon circulation [Lau and Kim, 2006].

[50] This study clearly indicates that: (1) anthropogenic aerosol have played a nonnegligible, and maybe even a leading, role in both the thermal and hydrologic changes over India and China land masses over the latter half of the twentieth century; (2) it becomes critical to know what changes occurred in the aerosol distributions over this period in order to arrive at an accurate estimate of the anthropogenic aerosol role, an issue that the weak observational database for

this time period may never permit; and (3) it is vital to know equally the absorbing and the scattering optical depth changes to infer the proper contribution of the aerosols to surface air temperature and precipitation changes. An important caveat to the above when comparing with the observed climate change over the 1950–1990 period is the fact that GHG increases were not considered in this study; their effects can be expected to yield a warming which may have offset the aerosols' substantial role in these regions in the case of temperature and likely affect the precipitation magnitude as well.

[51] Sea-surface temperature was prescribed as a first step to isolate only the effects of aerosols. As a result, the modeled changes in the hydrologic cycle may not be capturing the quantitative details accurately (e.g., on decadal timescales). If SST changes due to aerosol loading changes yielded strong feedbacks, particularly with regard to clouds, this would further add to the complexity of the aerosol impacts. For example, the increased cloudiness associated with the absorbing HOD experiments could potentially further reduce the north-south SST gradient and serve to spin-down the monsoon circulation [Ramanathan *et al.*, 2005], counteracting the enhanced monsoon associated with the increase in aerosol absorption and associated shortwave atmospheric heating. However, as Lau *et al.* [2006] point out, absorbing aerosol impacts on the monsoon water cycle may be pertinent to interseasonal and interannual timescales. On these shorter timescales, variability in the monsoon is associated with the reversal of the meridional temperature gradient over the Tibetan Plateau, which is due to surface heating and rapid temperature rise over the Plateau in late spring and early summer [Li and Yanai, 1996]. In addition, Lestari and Iwasaki [2006] investigated the influences of SSTs and land surface temperatures on the Asian summer monsoon using a GCM and concluded that both land-sea thermal contrast and SST changes contribute to an enhancement of the monsoon circulation.

[52] Another limitation of this study is that aerosols are prescribed from off-line calculations and do not interact with the model dynamics. Assuming an external mixture of aerosols may impact this study for several reasons. First, black carbon is microphysically aged by other atmospheric aerosol and gaseous components through condensation and coagulation, which in turn is an effect that requires an interactive aerosol scheme. Secondly, internally mixing an absorbing aerosol species such as BC with scattering aerosol can enhance the efficiency of BC absorption [Fuller *et al.*, 1999]. However, we note that by considering a range of ω_o for both the LOD and HOD regimes based on observations, we have effectively mimicked the potential absorption enhancement due to internal mixing. Only the direct and semidirect effects of aerosols were considered in this study. Inclusion of the indirect effect would further complicate the relationship between aerosols and cloud amount and their associated surface solar flux changes.

[53] These experiments have been analyzed in only the boreal summer months because it is the period in which we are most likely to obtain a significant signal owing to increased aerosol absorption and optical depth, and because the HOD experiments have no seasonal cycle in the prescribed anthropogenic aerosol distributions. We note that black carbon aerosol forcing over India and the Tibetan

Table 7. June/July/August Change in HOD Temperature and Hydrologic Cycle Parameters Over Land^a

| | $\omega_o = 0.85^b$ | $\omega_o = 0.99^c$ |
|----------------------------|---------------------|---------------------|
| <i>India</i> | | |
| Δ Surface Temperature | D | ≈0 |
| Δ Tropospheric Temperature | I | D |
| Δ Lapse Rate | D | I |
| Δ(P – E) | I | D |
| Δ Groundwater | I | D |
| Δ Precipitable Water | I | D |
| Δ Low Cloud Amount | I | D |
| <i>China</i> | | |
| Δ Surface Temperature | D | D |
| Δ Tropospheric Temperature | I | D |
| Δ Lapse Rate | D | ≈0 |
| Δ(P – E) | I | D |
| Δ Groundwater | I | D |
| Δ Precipitable Water | I | D |
| Δ Low Cloud Amount | I | D |

^aI indicates increase relative to BASE; D indicates decrease.

^bAbsorbing HOD experiments (XCa and XCh).

^cScattering HOD experiment (XChW).

Plateau peaks in late spring, and pronounced increases of such aerosols could conceivably yield a statistically significant result even in spring or winter. Our conclusions, however, are based more upon the amount of scattering and absorbing aerosol present rather than the specificity of the aerosol species or their mixing state. The results from this study (e.g., the range exhibited by the sensitivity studies) concerning the dependence upon the scattering and absorbing aerosol material present are general enough that they can be extended to the dust aerosol species. We note that strong absorption from dust, though not considered here, persists into summer over the Tibetan Plateau. Depending on the optical characteristics, dust would have a similar effect as the absorbing aerosols considered here of enhancing monsoon circulation [e.g., *Lau et al.*, 2006]. However, dust, unlike SO₄ and BC, is not considered to be anthropogenic, and observations of dust optical properties and burdens over India and China are even less known than for other aerosol species.

[54] Despite these limitations, the central conclusions of this study are robust across the range in τ_e and τ_a investigated. The change in surface pressure relative to the BASE case and the resulting change in radiative effects, circulation, convergence, vertical motion, cloud amount, relative humidity, evaporation, and precipitation along with the surface energy budget provide a consistent picture that increases in anthropogenic aerosols in general, together with changes in the amount of absorbing aerosols in particular, may impact the hydrologic cycle and other related climate variables consistent with observations and other studies [e.g., *Menon et al.*, 2002; *Lau et al.*, 2006].

6. Conclusions

[55] Table 7 summarizes the sign change in land-area average temperature and hydrologic cycle parameters relative to the BASE case discussed in this study for the HOD regime. As the analyses and results in this study demonstrate, the fundamental uncertainty in the aerosol optical parameters τ_e and τ_a turns out to be of profound importance

for how the climate over the India and China land masses has been potentially affected by the absorbing and scattering anthropogenic aerosol components over approximately the second half of the twentieth century. The primary conclusions of this study are summarized as follows.

[56] 1. In both LOD and HOD regimes, increases (decreases) in cloud amount reinforce (counteract) the aerosol-induced surface solar flux reduction, impacting both surface air temperature and the surface energy balance. In the LOD regime, cloud amount generally decreases with increasing absorption (decreasing ω_o) arising in part owing to the semidirect effect. In the HOD regime, circulation changes serve to increase cloud amount when absorption is increased and decrease cloud amount when absorption decreases.

[57] 2. The changes in surface pressure relative to the BASE case (ΔP_{sfc} ; Figure 5) drive circulation changes that enhance or oppose the monsoon circulation of the control case, depending on the amounts of anthropogenic absorbing and scattering aerosols. An enhanced monsoon circulation associated with increased τ_a results in increased low-level convergence, increased upward motion, increased atmospheric water vapor, increased low-level cloud amount, and increased precipitation (particularly evident and statistically significant in the HOD regime). Conversely, in the nonabsorbing HOD simulation XChW, which has strong cooling over the Tibetan Plateau, the changes in surface pressure and 850-hPa winds are reversed and counteract the nominal monsoon circulation of the BASE case. As a result, precipitation is reduced over northern India, the northern Bay of Bengal, and most of China while precipitation increases over southeast Asia and the South China Sea.

[58] 3. The presence of atmospheric absorption leads to increased atmospheric water vapor while mostly scattering aerosols produce a decrease in precipitable water. Except for the nonabsorbing simulation (XChW), over land, RH and atmospheric stability increase over land as aerosol surface solar flux reduction cools the lower troposphere and BC absorption and latent heat flux warm the upper and middle troposphere. For the nonabsorbing HOD experiment (XChW), latent heat flux is reduced relative to the BASE case, and without absorbing BC aerosol, the entire atmospheric column over land cools.

[59] BC aerosol is projected to increase rapidly over India and China in the future while sulfate aerosol is projected to decrease [*Intergovernmental Panel on Climate Change*, 2001]. Decreasing BC aerosol will compensate for warming (less cooling) associated with decreased SO₄ [*Shindell et al.*, 2008; *Levy et al.*, 2008]. Our results indicate that if total anthropogenic aerosol loadings are large, reducing sulfate concentrations may have little effect on observed changes in the hydrologic cycle if absorbing black carbon is also not concomitantly reduced. This implies that, as attempts are made to improve air quality in the China and India land regions, in the context of potential climate impacts, they must consider reductions in both sulfate and black carbon aerosol in concert, together with the influences due to possible changes in dust.

[60] **Acknowledgments.** This report was prepared by C. A. Randles under award NA17RJ2612 from the National Oceanic and Atmospheric Administration, U.S. Department of Commerce. The statements, findings,

conclusion, and recommendations are those of the author(s) and do not necessarily reflect the views of the National Oceanic and Atmospheric Administration, or the U.S. Department of Commerce. Randles also acknowledges funding from the DOE Graduate Research Environmental Fellowship. We thank Hiram Levy II and Paul Ginoux for useful comments on the manuscript, M. Shekar Reddy, Dan Schwarzkopf, Yi Ming, and Larry Horowitz for assistance with the GCM, and Surabi Menon for providing AOD measurements over India and China and for helpful suggestions. We thank Brent Holben, S. N. Tripathi, Hong-Bin Chen, and Phillippe Goloub for their effort in establishing and maintaining the Kanpur, Kaashidhoo, and Beijing AERONET sites. We also thank three anonymous reviewers for their insights on improvements to the manuscript.

References

- Anderson, J., et al. (2004), The new GFDL global atmosphere and land model AM2-LM2: Evaluation with prescribed SST simulations, *J. Clim.*, *17*, 4641–4673.
- Babu, S. S., S. K. Satheesh, and K. K. Moorthy (2002), Aerosol radiative forcing due to enhanced black carbon at an urban site in India, *Geophys. Res. Lett.*, *29*(18), 1880, doi:10.1029/2002GL015826.
- Boer, G. J. (1993), Climate change and the regulation of the surface moisture and energy budgets, *Clim. Dyn.*, *8*(5), 225–239.
- Brohan, P., J. Kennedy, I. Harris, S. Tett, and P. D. Jones (2006), Uncertainty estimates in regional and global observed temperature changes: A new data set from 1850, *J. Geophys. Res.*, *111*, D12106, doi:10.1029/2005JD006548.
- Bush, B., and F. P. J. Valero (2003), Surface aerosol radiative forcing at Gosan during the ACE-Asia campaign, *J. Geophys. Res.*, *108*(D23), 8660, doi:10.1029/2002JD003233.
- Cess, R. (1985), Nuclear war: Illustrative effects of atmospheric smoke and dust upon solar radiation, *Clim. Change*, *7*(2), 237–251.
- Chang, C. P., Y. S. Zhang, and T. Li (2000), Interannual and interdecadal variations of the East Asian summer monsoon and tropical SSTs. Part I: Role of the subtropical ridge, *J. Clim.*, *13*, 4310–4325.
- Chen, C.-T., and V. Ramaswamy (1995), Parameterization of the solar radiative characteristics of low clouds and studies with a general circulation model, *J. Geophys. Res.*, *100*(D6), 11,611–11,622.
- Chen, C.-T., and V. Ramaswamy (1996), Sensitivity of simulated global climate to perturbations in low cloud microphysical properties. Part II: Spatially localized perturbations, *J. Clim.*, *9*, 2788–2801.
- Cheng, Y., U. Lohmann, and J. H. Zhang (2005), Contribution of changes in sea surface temperature and aerosol loading to the decreasing precipitation trend in southern China, *J. Clim.*, *18*, 1381–1390.
- Chung, C., and V. Ramanathan (2006), Weakening of the North Indian SST gradients and the monsoon rainfall in India and the Sahel, *J. Clim.*, *19*, 2036–2045.
- Chung, C., V. Ramanathan, and J. T. Kiehl (2002), Effects of the south Asian absorbing haze on the northeast monsoon and surface-air heat exchange, *J. Clim.*, *15*, 2462–2476.
- Chung, S., and J. H. Seinfeld (2005), Climate response of direct radiative forcing of anthropogenic black carbon, *J. Geophys. Res.*, *110*, D11102, doi:10.1029/2004JD005441.
- Chylek, P., and J. A. Coakley (1974), Aerosols and climate, *Science*, *183*, 75–77.
- Clarke, A. D., et al. (2004), Size distributions and mixtures of dust and black carbon aerosol in Asian outflow: Physiochemistry and optical properties, *J. Geophys. Res.*, *109*, D15509, doi:10.1029/2003JD004378.
- Coakley, J., and R. D. Cess (1985), Response of the NCAR Community Climate Model to the radiative forcing by the naturally-occurring tropospheric aerosol, *J. Atmos. Sci.*, *42*(16), 1677–1692.
- Collins, W., P. Rasch, B. Eaton, B. Khatatov, and J.-F. Lamarque (2001), Simulating aerosols using a chemical transport model with assimilation of satellite aerosol retrievals: Methodology for INDOEX, *J. Geophys. Res.*, *106*(D7), 7313–7336.
- Conant, W., J. Seinfeld, J. Wang, G. Carmichael, Y. Tang, I. Uno, P. Flatau, K. Markowicz, and P. K. Quinn (2003), A model for the radiative forcing during ACE-Asia derived from CIRPAS Twin Otter and R/V Ronald H. Brown data and comparison with observations, *J. Geophys. Res.*, *108*(D23), 8661, doi:10.1029/2002JD003260.
- Erlick, C., and V. Ramaswamy (2003), Sensitivity of the atmospheric lapse rate to solar cloud absorption in a radiative-convective model, *J. Geophys. Res.*, *108*(D16), 4522, doi:10.1029/2002JD002966.
- Erlick, C., V. Ramaswamy, and L. Russell (2006), Differing regional responses to a perturbation in solar cloud absorption in the SKYHI general circulation model, *J. Geophys. Res.*, *111*, D06204, doi:10.1029/2005JD006491.
- Feng, S., and Q. Hu (2005), Regulation of Tibetan Plateau heating on variation of the Indian summer monsoon in the last two millennia, *Geophys. Res. Lett.*, *32*, L02702, doi:10.1029/2004GL021246.
- Fitzgerald, J. (1975), Approximation formulas for the equilibrium size of an aerosol particle as a function of its dry size and composition and the ambient relative humidity, *J. Appl. Meteorol.*, *14*, 1044–1049.
- Fu, Q., and C. M. Johanson (2005), Satellite-derived vertical dependence of tropical tropospheric temperature trends, *Geophys. Res. Lett.*, *32*, L10703, doi:10.1029/2004GL022266.
- Fuller, K., W. Malm, and S. M. Kreidenweis (1999), Effects of mixing on extinction by carbonaceous particles, *J. Geophys. Res.*, *104*(D13), 15,941–15,954.
- Ginoux, P., L. Horowitz, V. Ramaswamy, I. Geogdzhayev, B. Holben, G. Stenchikov, and X. Tie (2006), Evaluation of aerosol distribution and optical depth in the Geophysical Fluid Dynamics Laboratory coupled model CM2.1 for present climate, *J. Geophys. Res.*, *111*, D22210, doi:10.1029/2005JD006707.
- Gu, Y., K. Liou, Y. Xue, C. Mechoso, W. Li, and Y. Luo (2006), Climatic effects of different aerosol types in China simulated by the UCLA general circulation model, *J. Geophys. Res.*, *111*, D15201, doi:10.1029/2005JD006312.
- Hansen, J., and L. Nazarenko (2004), Soot climate forcing via snow and ice albedos, *Proc. Natl. Acad. Sci. U. S. A.*, *101*, 423–428, doi:10.1073/pnas.2237157100.
- Hansen, J., M. Sato, and R. Ruedy (1997), Radiative forcing and climate response, *J. Geophys. Res.*, *102*(D6), 6831–6864.
- Haywood, J., and V. Ramaswamy (1998), Global sensitivity studies of the direct radiative forcing due to anthropogenic sulfate and black carbon aerosols, *J. Geophys. Res.*, *103*(D6), 6043–6058.
- Haywood, J. M., V. Ramaswamy, and B. J. Soden (1999), Tropospheric aerosol climate forcing in clear-sky satellite observations over the oceans, *Science*, *283*, 1299–1303.
- Holben, B., et al. (2001), An emerging ground-based aerosol climatology: Aerosol optical depth from AERONET, *J. Geophys. Res.*, *106*(D11), 12,067–12,097.
- Horowitz, L. (2006), Past, present, and future concentrations of tropospheric ozone and aerosols: Methodology, ozone evaluation, and sensitivity to aerosol wet removal, *J. Geophys. Res.*, *111*, D22211, doi:10.1029/2005JD006937.
- Huang, Y., W. L. Chameides, and R. E. Dickinson (2007), Direct and indirect effects of anthropogenic aerosols on regional precipitation over east Asia, *J. Geophys. Res.*, *112*, D03212, doi:10.1029/2006JD007114.
- Huebert, B., T. Bates, P. Russell, G. Shi, Y. Kim, K. Kawamura, G. Carmichael, and T. Nakajima (2003), An overview of ACE-Asia: Strategies for quantifying the relationships between Asian aerosols and their climate impacts, *J. Geophys. Res.*, *108*(D23), 8633, doi:10.1029/2003JD003550.
- Intergovernmental Panel on Climate Change (2001), *Climate Change 2001: The Scientific Basis*, edited by J. T. Houghton et al., Cambridge Univ. Press, Cambridge, U.K.
- Johnson, B., K. Shine, and P. M. Forster (2004), The semi-direct aerosol effect: Impact of absorbing aerosols on marine stratocumulus, *Q. J. R. Meteorol. Soc.*, *Part B*, *130*(599), 1407–1422.
- Kim, D.-H., B. Sohn, T. Nakajima, and T. Takamura (2005), Aerosol radiative forcing over east Asia determined from ground-based solar radiation measurements, *J. Geophys. Res.*, *110*, D10S22, doi:10.1029/2004JD004678.
- Lau, K., and K. Kim (2006), Observational relationships between aerosol and Asian monsoon rainfall and circulation, *Geophys. Res. Lett.*, *33*, L21810, doi:10.1029/2006GL027546.
- Lau, K., M. Kim, and K. Kim (2006), Asian summer monsoon anomalies induced by aerosol direct forcing: The role of the Tibetan Plateau, *Clim. Dyn.*, *26*(7–8), 855–864.
- Lazante, J., et al. (2006), What do observations indicate about the changes of temperature in the atmosphere and at the surface since the advent of measuring temperatures vertically?, in *US Climate Change Science Program Synthesis and Assessment Product 1.1: Temperature Trends in the Lower Atmosphere*, edited by T. Karl, S. Hassol, C. Miller, and W. L. Murray, chap. 3, pp. 47–70, NOAA, Silver Spring, Md.
- Lee, K. H., Z. Li, M. S. Wong, J. Xin, Y. Wang, W.-M. Hao, and F. Zhao (2007), Aerosol single scattering albedo estimated across China from a combination of ground and satellite measurements, *J. Geophys. Res.*, *112*, D22S15, doi:10.1029/2007JD009077.
- Lestari, R., and T. Iwasaki (2006), A GCM study on the roles of the seasonal marches of the SST and land-sea thermal contrast in the onset of the Asian summer monsoon, *J. Meteorol. Soc. Jpn.*, *84*(1), 69–83.
- Levy, H., II, M. D. Schwarzkopf, L. Horowitz, V. Ramaswamy, and K. Findell (2008), Strong sensitivity of late 21st century climate to projected changes in short-lived air pollutants, *J. Geophys. Res.*, *113*, D06102, doi:10.1029/2007JD009176.
- Li, C. F., and M. Yanai (1996), The onset and interannual variability of the Asian summer monsoon in relation to land sea thermal contrast, *J. Clim.*, *9*, 358–375.

- Lin, S.-J. (2004), A “vertically Lagrangian” finite-volume dynamical core for global models, *Mon. Weather Rev.*, *132*(10), 2293–2307.
- Luo, Y., D. Lu, X. Zhou, W. Li, and Q. He (2001), Characteristics of the spatial distribution and yearly variation of aerosol optical depth over China in the last 30 years, *J. Geophys. Res.*, *106*(D13), 14,501–14,513.
- Markowicz, K., P. Flatau, P. Quinn, C. Carrico, M. Flatau, A. Vogelmann, D. Bates, M. Liu, and M. J. Rood (2003), Influence of relative humidity on aerosol radiative forcing: An ACE-Asia experiment perspective, *J. Geophys. Res.*, *108*(D23), 8662, doi:10.1029/2002JD003066.
- Menon, S., J. Hansen, L. Nazarenko, and Y. Luo (2002), Climate effects of black carbon aerosols in China and India, *Science*, *297*, 2250–2253.
- Nakajima, T., et al. (2003), Significance of direct and indirect radiative forcings of aerosols in the East China Sea region, *J. Geophys. Res.*, *108*(D23), 8658, doi:10.1029/2002JD003261.
- Pant, P., P. Hegde, U. Drmka, R. Sagar, S. Satheesh, K. Moorthy, A. Saha, and M. K. Srivastava (2006), Aerosol characteristics at a high-altitude location in central Himalayas: Optical properties and radiative forcing, *J. Geophys. Res.*, *111*, D17206, doi:10.1029/2005JD006768.
- Peixoto, J., and A. H. Oort (1992), *Physics of Climate*, Am. Inst. of Phys., New York, NY.
- Ramana, M. V., V. Ramanathan, I. A. Podgorny, B. B. Pradhan, and B. Shrestha (2004), The direct observations of large aerosol radiative forcing in the Himalayan region, *Geophys. Res. Lett.*, *31*, L05111, doi:10.1029/2003GL018824.
- Ramanathan, V., and G. Carmichael (2008), Global and regional climate changes due to black carbon, *Nat. Geosci.*, *1*, 221–227.
- Ramanathan, V., P. Crutzen, J. Kiehl, and D. Rosenfeld (2001a), Atmosphere—Aerosols, climate, and the hydrological cycle, *Science*, *294*, 2119–2124.
- Ramanathan, V., et al. (2001b), Indian Ocean Experiment: An integrated analysis of the climate forcing and effects of the great Indo-Asian haze, *J. Geophys. Res.*, *106*(D22), 28,371–28,398.
- Ramanathan, V., et al. (2005), Atmospheric brown clouds: Impacts on south Asian climate and hydrological cycle, *Proc. Natl. Acad. Sci. U. S. A.*, *102*, 5326–5333.
- Ramaswamy, V., and J. T. Kiehl (1985), Sensitivities of the radiative forcing due to large loadings of smoke and dust aerosols, *J. Geophys. Res.*, *90*(D3), 5597–5613.
- Ramaswamy, V., et al. (2001), Radiative forcing of climate change, in *Climate Change 2001: The Scientific Basis*, edited by J. T. Houghton et al., pp. 351–406, Cambridge Univ. Press, Cambridge, U.K.
- Reynolds, R. W., N. A. Rayner, T. M. Smith, D. C. Stokes, and W. Wang (2002), An improved in situ and satellite SST analysis for climate, *J. Clim.*, *15*, 1609–1625.
- Satheesh, S., and V. Ramanathan (2000), Large differences in tropical aerosol forcing at the top of the atmosphere and Earth’s surface, *Nature*, *405*(6782), 60–63.
- Shindell, T., H. Levy, M. D. Schwarzkopf, L. W. Horowitz, J.-F. Lamarque, and G. Faluvegi (2008), Multi-model projections of climate change from short-lived emissions due to human activities, *J. Geophys. Res.*, *113*, D11109, doi:10.1029/2007JD009152.
- Solomon, S., et al. (2007), Technical summary, in *Climate Change 2007: The Physical Science Basis, Contribution of Working Group I to the Fourth Assessment Report of the Intergovernmental Panel on Climate Change*, pp. 21–87, Cambridge Univ. Press, Cambridge, U.K.
- Takamura, T., N. Sugimoto, A. Shimizu, A. Uchiyama, A. Yamazaki, K. Aoki, T. Nakajima, B. J. Sohn, and H. Takenaka (2007), Aerosol radiative characteristics at Gosan, Korea, during the Atmospheric Brown Cloud East Asian Regional Experiment 2005, *J. Geophys. Res.*, *112*, D22S36, doi:10.1029/2007JD008506.
- Tripathi, S. N., S. Dey, V. Tare, and S. K. Satheesh (2005), Aerosol black carbon radiative forcing in an industrial city in northern India, *Geophys. Res. Lett.*, *32*, L08802, doi:10.1029/2005GL022515.
- Wetherald, R., and S. Manabe (1988), Cloud feedback processes in a general circulation model, *J. Atmos. Sci.*, *45*(8), 1397–1415.
- Wu, J., W. Jiang, C. Fu, B. Su, H. Liu, and J. Tang (2004), Simulation of the radiative effect of black carbon aerosols and the regional climate responses over China, *Adv. Atmos. Sci.*, *21*(4), 637–649.
- Zhao, C., X. Tie, and Y. Lin (2006), A possible feedback of reduction of precipitation and increase in aerosols over eastern central China, *Geophys. Res. Lett.*, *33*, L11814, doi:10.1029/2006GL025959.

V. Ramaswamy, Geophysical Fluid Dynamics Laboratory, 201 Forrestal Road, Princeton, NJ 08540, USA. (V.Ramaswamy@noaa.gov)
 C. A. Randles, NASA Goddard Space Flight Center, Code 613.3, Building 33 Room 311, Mailstop 613.3, Greenbelt, MD 20771, USA. (crandles@umbc.edu)